J. Fluid Mech. (2023), *vol*. 976, A32, doi:10.1017/jfm.2023.933

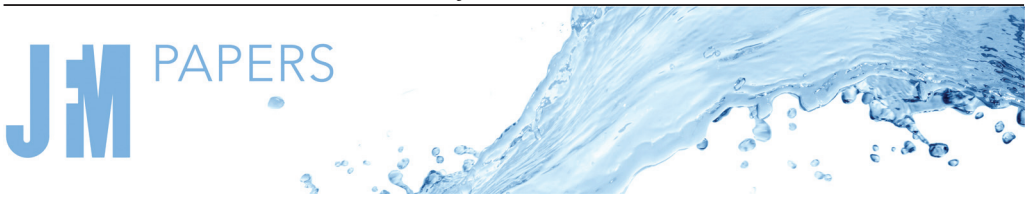

Flow topology in the gap and wake of convex curved tandem cylinders

Tale E. Aasland[1],†, **Bjørnar Pettersen**[1], **Helge I. Andersson**[1] and **Fengjian Jiang**[2]

[1]Department of Marine Technology, Norwegian University of Science and Technology, NO-7491 Trondheim, Norway

[2]SINTEF Ocean, NO-7052 Trondheim, Norway

(Received 14 June 2023; revised 14 September 2023; accepted 3 November 2023)

Flow around curved tandem cylinders in the convex configuration has been studied by means of direct numerical simulations, for a Reynolds number of 500 and a nominal gap ratio of 3.0. Spanwise variation of flow regimes, as well as curvature-induced axial velocity, leads to an exceedingly complex vortex dynamics in the wake. Both parallel and oblique vortex shedding are observed. Oblique shedding is connected to repeated occurrences of dislocations. The dislocations are caused by two main mechanisms: frequency differences in the upper part of the curved geometry and shedding of gap vortices into the lower near wake. Both types of dislocations are closely associated with a mode switch in the gap. In parts of the gap, there is low-frequency quasi-periodic asymmetry of the gap vortices, where the flow is biased to one side of the gap for intervals of several wake vortex shedding periods. The switch from side to side is associated with a surge of the vertical velocity, and the frequency of the switch is similar to that of long-term variation of the recirculation length in the lower gap.

Key words: vortex dynamics, vortex interactions, vortex shedding

1. Introduction

The flow around multiple curved geometries covers highly interesting fundamental flow physics, and the topic has high relevance from an engineering point of view. The study of tandem curved cylinders encompasses both these perspectives. To date there are only two studies that investigate dual curved cylinders (Gao *et al.* 2021; Aasland *et al.* 2022*a*).

† Email address for correspondence: tale.e.aasland@ntnu.no

Therefore, an introduction to flow around a single curved cylinder is given; a geometry which has become the topic of quite a large number of studies in recent years.

Some basic concepts of the flow around two straight cylinders in tandem are also relevant when discussing the present results, and these are introduced in § 1.2.

1.1. *Single curved cylinders*

The major difference between a straight and a curved cylinder is the existence of curvature-induced flow along the cylinder axis, which influences the wake topology and forces acting on the curved cylinder. The direction and strength of the axial flow depend strongly on the inflow direction with respect to the plane of curvature. Therefore, the flow topology can change fundamentally with variation of the inflow direction (Miliou, Sherwin & Graham 2003*a*,*b*; Miliou *et al.* 2007; Ahmed 2010; Lee, Paik & Srinil 2020). Directing the incoming flow towards the outer face of the cylinder (convex configuration) results in a thoroughly different wake dynamics than directing it towards the inner face (concave configuration). Because the object of the present study is to investigate fixed curved tandem cylinders in the convex configuration, concave and oblique configurations are excluded from the present review, as are studies of vortex-induced vibrations of curved cylinders. Comprehensive studies of the concave configuration were carried out by, among others, Miliou *et al.* (2007), Shang *et al.* (2018), Jiang, Pettersen & Andersson (2018*a*, 2019), Jiang *et al.* (2018*b*), Chiatto *et al.* (2021, 2023) and Lee *et al.* (2020), who investigated a curved cylinder at several inflow angles. Vortex-induced vibration of curved cylinders was studied by de Vecchi, Sherwin & Graham (2008), Assi *et al.* (2014), Seyed-Aghazadeh, Budz & Modarres-Sadeghi (2015), Seyed-Aghazadeh *et al.* (2021), Srinil, Ma & Zhang (2018) and Ma & Srinil (2023).

Superficially, the wake of a single curved cylinder in the convex configuration is similar to that of a straight cylinder, as both wakes exhibit a von Kármán vortex street (see figure 1). One might perhaps have expected cellular shedding in the curved case, due to phase differences stemming from the local curvature, similar to the wake behind a tapered cylinder (Narasimhamurthy, Andersson & Pettersen 2009). Miliou *et al.* (2007), however, showed that, with the exception of a Reynolds number of 100 ($Re = U_0 D/\nu$, where U_0 is the inflow velocity, D is the cylinder diameter and ν is the kinematic viscosity), the vortices are in phase along the span, with no spanwise variation of the Strouhal number ($St = f_v D/U_0$, where f_v is the vortex shedding frequency). This result is related to weakening of the vortex strength with increasing axial flow. Strong axial flow in the lower part of the near wake inhibits communication between the shear layers, similar to a splitter plate (Cardell 1993), resulting in a weaker swirling flow. A similar non-shedding regime was described by Ramberg (1983) for a straight cylinder with inclination. Contrary to the lower wake, the spanwise vortices in the upper part of the wake, where the cylinder axis is nearly normal to the incoming flow, maintain a strength comparable to a straight cylinder. Thus, the wake is driven by the upper vortices. For a given Reynolds number, these vortices have a dominant frequency close to that of a straight cylinder (Miliou *et al.* 2007).

The orientation of the spanwise vortex cores can be normal to the incoming flow or inclined to align with the local curvature. Miliou *et al.* (2007) found straight cores at a Reynolds number of 100, and moderately inclined cores for $Re = 500$, as illustrated in figure 1(*a*). They suggested that the vortex cores align increasingly with the local curvature as the Reynolds number increases, which was corroborated by the results by Gallardo, Andersson & Pettersen (2014) at $Re = 3900$.

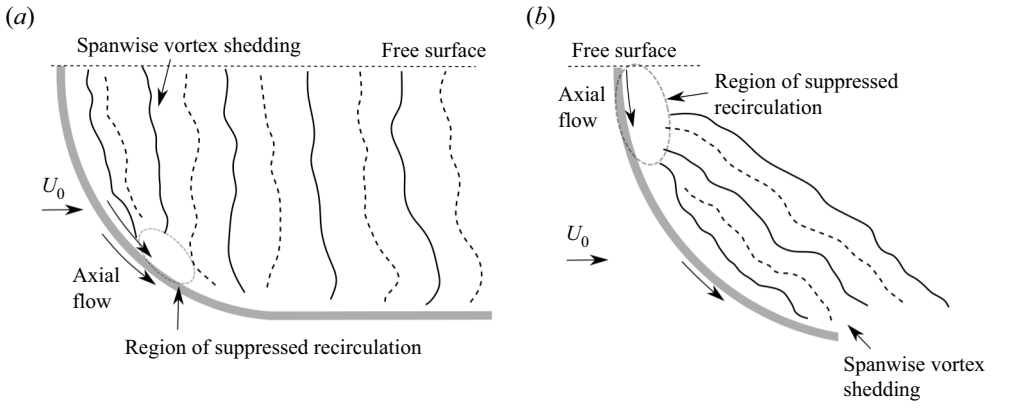

Figure 1. Schematic of the flow around convex curved cylinders. Adapted from flow visualisations by (*a*) Miliou *et al.* (2007) and (*b*) Shang, Stone & Smits (2018). The Reynolds numbers were 500 and 486, and the radii of curvature 12.5 and 22.9, respectively. The solid and dashed lines represent the cores of oppositely rotating vortex cells.

The axial flow can be quite significant. For instance, Miliou *et al.* (2007) estimated the downwards-deflected flow rate along the stagnation face to be approximately one third of the total flow rate. Because of the axial flow, the top boundary condition, be it numerical or experimental, is important. Shang *et al.* (2018) discovered that, in their experiment, vortex shedding was inhibited within a distance of up to 6*D* away from the free surface, depending on the radius of curvature (concave cylinder). A corresponding result was found in numerical simulations by Gallardo, Pettersen & Andersson (2013). It was discovered that the free-slip condition on the top boundary of the computational domain influenced the vertical velocity component unless a straight 6*D* long vertical extension was added to the upper geometry. When the extension was included, a mild upwelling was allowed to develop behind the upper part of the curved cylinder, which extended upwards along the straight part of the geometry.

With the inclusion of a straight vertical extension, spanwise vortex dislocations began to occur in the simulations of Gallardo *et al.* (2014). Such dislocations arise when local frequency and/or phase differences cause neighbouring vortex cells to move out of phase with each other, resulting in complex linking patterns between the vortex cores (Williamson 1989). In the wake of a straight cylinder, vortex dislocations develop spontaneously when the spanwise length is sufficient (Henderson 1997). This phenomenon may occur anywhere along the span, and the location varies with time. In the curved cylinder case, however, the dislocations always occurred near the intersection between the curved part and the straight vertical extension, and propagated downwards into the wake. It was discovered that the two cylinder parts had slightly different Strouhal numbers, and this was believed to be the cause of the dislocations (Gallardo *et al.* 2014).

An important question for investigations into curved cylinder flow has been the applicability of the independence principle for such geometries. The independence principle relies on the assumption that only the normal inflow component is important to the vortex dynamics, and that the axial flow can be neglected. For a curved cylinder, the constant change in local curvature would result in a different local Strouhal number for every section along the span, using this assumption. Thus, the validity of the independence principle was in essence refuted for a curved cylinder by Miliou *et al.* (2007), given that their results showed constant *St* along the span. However, Gallardo *et al.* (2014)

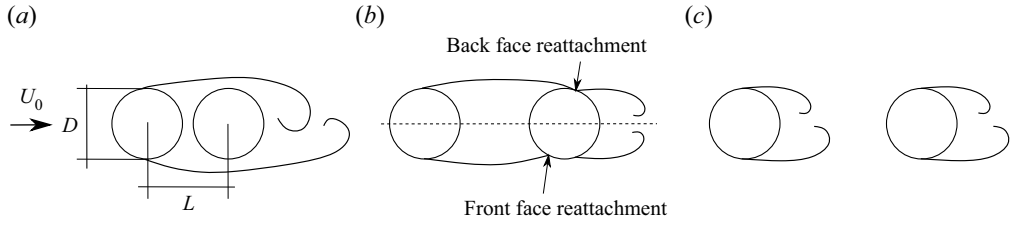

Figure 2. The main flow regimes of straight tandem cylinders: (*a*) overshoot/no reattachment, (*b*) reattachment and (*c*) co-shedding. Reattachment may occur on the back face or the front face of the downstream cylinder.

showed that the independence principle was valid along the upper part of the cylinder. The base pressure coefficient computed according to this principle began to deviate from the actual values approximately at the mid-span of the curved part of the geometry. The deviation point corresponded with the upper boundary of the region where recirculation was suppressed by the axial flow. Based on this result, a distinction between the upper and lower wake was suggested.

1.2. *Straight tandem cylinders*

Tandem cylinder flow comprises three main flow regimes: overshoot, reattachment and co-shedding, as shown in figure 2. Within the overshoot regime, the upstream cylinder shear layers envelop the downstream cylinder and roll up in the wake, so that shedding is controlled by the upstream cylinder. When the gap spacing between the cylinders increases, the upstream cylinder shear layers begin to reattach onto the downstream cylinder. Shedding now occurs from the downstream cylinder alone. A further increase of the cylinder spacing leads to an upstream movement of the reattachment point, until finally, the upstream shear layers detach from the downstream cylinder, and shedding of large-scale vortices occurs from both cylinders. Tandem cylinder flow regimes are normally discussed in terms of the gap ratio, L/D, where L is the centre to centre spacing between the cylinders, and D is the cylinder diameter.

Because the shear layers and the entrainment demands of large-scale vortex formation are sensitive to the inflow velocity, the tandem cylinder regimes are Reynolds number dependent. This makes it challenging to characterise the different regimes by means of the gap ratio alone. Nevertheless, Zdravkovich (1987) suggested the following classification, which is still in wide use: overshoot $1.0 \leq L/D \leq 1.2$–1.8, reattachment 1.2–$1.8 \leq L/D \leq 3.4$–3.8 and co-shedding 3.4–$3.8 \leq L/D$. Due to the Reynolds number dependency, Xu & Zhou (2004) later proposed that, instead of a range of gap ratios, the flow regimes of tandem cylinders should be described by means of ranges of Reynolds number and gap ratio combinations.

The gap ratio where co-shedding commences is traditionally called the critical spacing, L_c/D, or the drag-inversion spacing. The latter term refers to the fact that recirculation in the gap (which occurs during reattachment) leads to suction, resulting in a negative drag coefficient for the downstream cylinder. When there is shedding from both cylinders, the sign of the downstream cylinder drag coefficient is reversed, and becomes positive; hence ‘drag inversion’. The critical spacing typically varies between 3.0 and 5.0 (Okajima 1979; Igarashi 1981; Xu & Zhou 2004; Alam 2014), depending on the Reynolds number and other factors, such as free-stream turbulence (Ljungkrona, Norberg & Sunden 1991) or inflow gust amplitude (Wang *et al.* 2022).

Reattachment of the upstream cylinder shear layers may be alternating, quasi-steady/symmetric or intermittent (Zdravkovich 1987). Alternating reattachment means that one shear layer reattaches, while the other overshoots the downstream cylinder. Within the reattachment regime, recirculating vortices form in the gap between the cylinders. For lower gap ratios, these are symmetric (Lin, Yang & Rockwell 2002). As the gap ratio is increased, the recirculating vortices become asymmetric/alternating (Lin *et al.* 2002; Zhou *et al.* 2019). Because they are restrained by the presence of the downstream cylinder, these vortices form repeatedly at the same streamwise location, whether they are symmetric or alternating. Therefore, they are typically dubbed quasi-stationary or quasi-steady in the literature. Herein, we simply call them 'gap vortices'.

The transition between tandem cylinder flow regimes is subject to bi-stability, meaning that the flow intermittently jumps between regimes. Intermittent overshoot/reattachment was found by Xu & Zhou (2004), but has, to our knowledge, not been reported by others. Intermittent reattachment/co-shedding, however, is reported in a number of studies (Igarashi 1981; Xu & Zhou 2004; Kitagawa & Ohta 2008; Alam 2014; Afgan *et al.* 2023). When the term 'bi-stability' is used in the context of tandem cylinders, it usually refers to the jump between reattachment and co-shedding.

Igarashi (1981) reported that the bi-stable regime starts when the gap vortices become unstable, and shedding occurs intermittently (labelled regime D in that study). For a given Reynolds number, intervals of shedding in the gap became more frequent, with longer duration, as the gap ratio was increased. Bi-stability manifests itself as two distinct velocity spectral peaks, of similar magnitude. In Igarashi's (1981) study, for a given gap ratio, these peaks start out close to one another, and gradually separate as the Reynolds number is increased.

The three-dimensionality of the gap and wake is important, in particular at moderate Reynolds numbers. Deng *et al.* (2006), Papaioannou *et al.* (2006) and Carmo & Meneghini (2006) all concluded that two-dimensional simulations failed to predict the correct drag-inversion spacing for a three-dimensional wake. Moreover, Papaioannou *et al.* (2006) discovered that there are strong spanwise phase variations in the gap and wake within the reattachment regime, with a clear periodic spanwise structure. A similar result was recently reported by Wang *et al.* (2021), for channel-confined tandem cylinders. The results of Aasland *et al.* (2022*b*) indicated the possibility of spanwise localised bi-stability near the critical spacing, where shedding in the gap occurs in spanwise cells. This was confirmed by Aasland *et al.* (2023), who found that bi-stability manifests not only spanwise localised, but also asymmetrically in the gap; shedding may occur repeatedly from just one gap shear layer.

For further details, the reader is encouraged to peruse the comprehensive reviews of Sumner (2010), and Zhou & Alam (2016).

1.3. *Motivation for the present investigation*

Due to their relevance to the aerospace industry (typically as simplified configurations of aircraft landing gear), non-parallel tandem cylinders have been investigated by several researchers (Thakur, Liu & Marshall 2004; Wilkins, Hogan & Hall 2013; Younis, Alam & Zhou 2016; Alam *et al.* 2022), but there are still very few investigations concerning curved dual cylinders. The lack of literature is possibly due to the complexity of the subject. Meticulous attention to the set-up is required, and in the case of numerical investigations, the demand on grid refinement is large. Gao *et al.* (2021) investigated side-by-side cylinders at different spacings, for Reynolds numbers of 100 and 500. The study of Zhu *et al.* (2019) is concerned with a symmetrical, hanging riser segment of

different curvatures (i.e. different distances between the end points), at a Reynolds number of 100. For high curvatures, the cylinder end segments are close enough that the flow resembles that of tandem cylinders, with a concave cylinder in the wake of a convex one.

An initial study of curved tandem cylinders at a gap ratio of 3.0 was conducted by Aasland *et al.* (2022*a*), which was concerned mainly with the forces. Spanwise variation of tandem flow regimes, due to a gradual change in the effective gap ratio along the span, was discovered. There was low-frequency variation of the drag coefficients, and it was suggested that this may be caused by a slow meandering of the location at which gap vortex shedding starts.

The aim of the present study is to characterise the flow topology of the gap and wake; in particular, intricate interaction between these two flow regions, and how bi-stability in the gap influences the wake region. Moreover, the source of the low-frequency variations described by Aasland *et al.* (2022*a*) is investigated, along with the hypothesis of meandering gap shedding inception.

2. Flow problem formulation and computational aspects

The present geometry consists of two curved tandem cylinders of equal diameter, with the inflow in the plane of curvature of the cylinders. The convex configuration is studied, and the gap ratio is $L/D = 3.0$. A Reynolds number of 500 was chosen, based on previous investigations with a single and dual curved cylinders (Miliou *et al.* 2007; Jiang *et al.* 2018*a*,*b*; Lee *et al.* 2020; Gao *et al.* 2021; Aasland *et al.* 2022*a*). For this combination of gap ratio and Reynolds number, alternating overshoot/reattachment is expected for straight tandem cylinders (Aasland *et al.* 2023), with the three-dimensional gap/wake instability mode T3 (Carmo, Meneghini & Sherwin 2010*a*).

2.1. *Governing equations and numerical method*

In the present study, the full Navier–Stokes equations for incompressible flow are solved by means of direct numerical simulations (DNS)

$$\frac{\partial u_i}{\partial x_i} = 0, \tag{2.1}$$

$$\frac{\partial u_i}{\partial t} + u_j \frac{\partial u_i}{\partial x_j} = -\frac{1}{\rho}\frac{\partial P}{\partial x_i} + \frac{\partial}{\partial x_j}\left(\nu\left[\frac{\partial u_i}{\partial x_j} + \frac{\partial u_j}{\partial x_i}\right]\right), \quad i,j = 1,2,3, \tag{2.2}$$

where u is velocity and P is pressure. All simulations were carried out using the MGLET (multi grid large eddy turbulence) flow solver. MGLET is based on a finite volume formulation of the incompressible Navier–Stokes equations, and uses a staggered Cartesian grid (Manhart 2004). Solid bodies are introduced through an immersed boundary method (Peller *et al.* 2006), where the boundary is discretised using a cut-cell approach (Unglehrt *et al.* 2022). A third-order low-storage explicit Runge–Kutta time integration scheme is used for time stepping, and the Poisson equation is solved using an iterative, strongly implicit procedure. MGLET has previously been used for convex (Gallardo *et al.* 2014; Aasland *et al.* 2022*a*) and concave (Jiang *et al.* 2018*a*, 2019) curved cylinder studies.

Free-slip boundary conditions are used on all computational domain boundaries except the inlet and outlet. Uniform inflow is imposed at the inlet, and a Neumann condition is imposed on the velocity components at the outlet. No-slip and impermeability conditions were enforced on the cylinder surfaces.

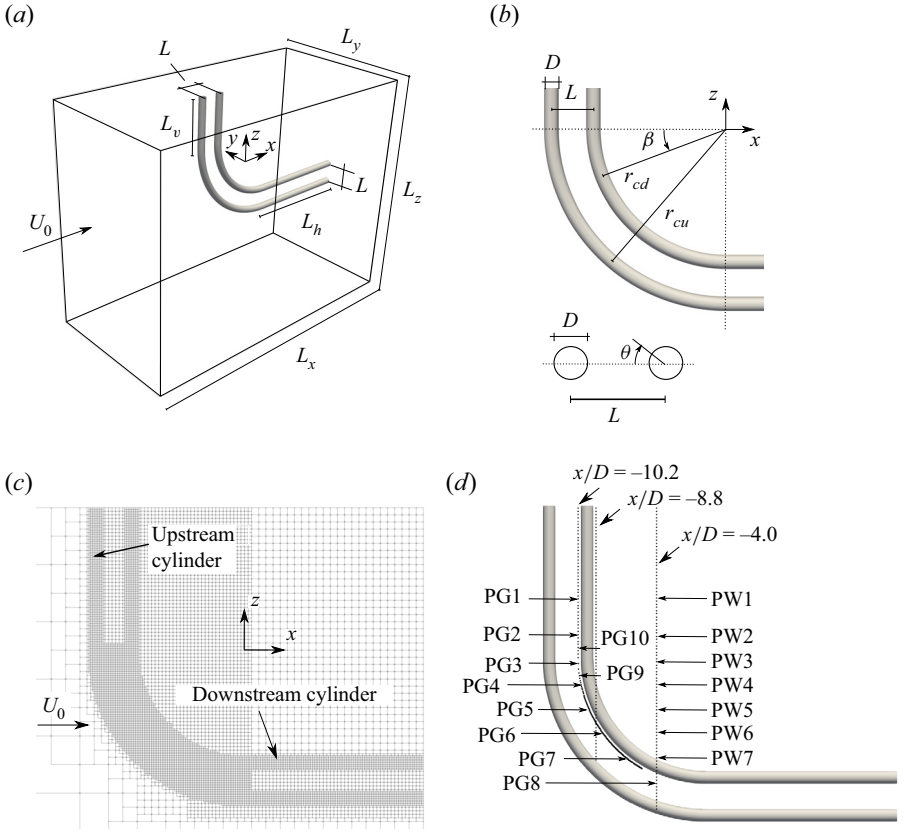

Figure 3. (*a*) Computational domain, (*b*) definitions, (*c*) computational grid schematic and (*d*) location of velocity probes. Probes PG1–7 are on the same z/D levels as their counterparts in the wake PW1–7, ranging from $z/D = 5$ to $z/D = -8$. PG8, PG9 and PG10 are located at $z/D = -10$, -1.2 and 1.0, respectively.

During the first 650 time units tU_0/D, the time step was gradually adjusted to obtain a target Courant number of 0.6. The final time step was $dt = 0.00247D/U_0$. After initialisation, sampling of statistics was carried out for 3150 time units, which corresponds to approximately 450 large-scale vortex shedding cycles. The long initialisation and sampling times are required due to low-frequency variations in the flow field, similar to the findings of previous studies (Gallardo *et al.* 2014; Aasland *et al.* 2022*a*).

Herein, all reported frequencies are based on discrete Fourier transform of velocity time traces sampled at probe lines in the gap and wake, as shown in figure 3(*d*). Vertical wake probe lines were located along $(x/D, y/D) = (-4.0, 0.0)$ and $(-8.8, 0.0)$. In the gap, the probes were always located $0.2D$ away from the downstream cylinder stagnation point, at $y/D = 0$, spanning $-9.0 \leq z/D \leq 12.0$. The internal probe spacing was $0.25D$ in the wake and the vertical part of the gap. In the curved part of the gap, the spacing was $0.03125D$. The frequency resolution can be computed as $\mathrm{d}f = 1/(\mathrm{d}t \times Nt)$, where Nt is the number of sampling points in the time series. Probe data were sampled at every time step, which means $Nt = 3150/\mathrm{d}t$, so that $\mathrm{d}f = 1/3150 = 3.16 \times 10^{-4}$. Because the geometry is fully three-dimensional, spanwise averaging of spectra (commonly used for straight cylinders), is not appropriate in the present case. Therefore, spectral noise was reduced by means of Welch's method, using a Hamming window with 50 % overlap. *In situ* fast Fourier transform (FFT) analysis was carried out, in order to investigate the

distribution of certain frequencies within the flow. The advantage of this method, which is carried out as an integrated part of the simulations, is that the analysis does not depend on specific probes; the results are given for the entire computational domain. The drawback is that the frequencies to be investigated must be specified in advance, and they must all be integer multiples of the lowest specified frequency. Moreover, they cannot be changed without restarting sampling of statistics. For these reasons, *in situ* FFT was first carried out during the main simulation, using a first guess of frequencies. This gave a spectral map of frequencies that were fairly close to the frequencies measured by the probes, although not completely accurate. Then, a new simulation was started from the flow field of the main simulation and run for 150 time units, using target frequencies that were adjusted according to the probe data. This resulted in a more accurate spectral map for the *in situ* FFT, although with the drawback of a shorter sampling time.

2.2. *Geometry, computational domain and grid*

The curved part of each cylinder is a quarter segment of ring with a radius of curvature r_c. The upstream cylinder has a radius of curvature of $r_{cu} = 12.5D$, similar to previous studies with a single curved cylinder (Miliou *et al.* 2007; Gallardo *et al.* 2014). In order to ensure a constant gap ratio along the entire geometry, a curvature of $r_{cd} = 9.5D$ is used for the downstream cylinder. Due to the uniform inflow condition, the effective gap ratio varies along the curved part of the cylinders. Therefore, the chosen gap ratio is referred to as the nominal gap ratio henceforth.

To minimise the influence from the computational boundaries, the curved tandem cylinders were fitted with straight vertical extensions of $L_v = 12D$, as well as horizontal extensions of $L_h = 15D$. An evaluation of the required vertical extension length was carried out, and the results are shown in the Appendix.

The computational domain and geometry are depicted in figure 3, as well as a schematic representation of the grid structure. The total domain size is $43D$, $24D$ and $43.2D$ in the x, y and z directions, respectively.

A detailed grid refinement study was carried out by Aasland *et al.* (2022*a*). It was found that the flow was significantly influenced by the refinement level in the curved part of the gap, where the velocity and pressure gradients are strong. Thus, the final grid featured a refinement of this region to the same grid cell size as in the boundary layers near the solid bodies. The same grid resolution and refinement regions are used in the present study, the only difference being a longer L_v. The smallest element size is $\mathrm{d}x = \mathrm{d}y = \mathrm{d}z = 0.0075D$, which is also the grid resolution inside the boundary layer. The total number of elements is approximately 704×10^6.

2.3. *Definitions*

Herein, the x, y and z directions are referred to as streamwise, cross-flow and vertical. Vortices that align with the vertical direction are dubbed spanwise. When vortex shedding modes are discussed, 'parallel' means that the spanwise orientation of the vortices is parallel to the straight vertical extension, i.e. normal to the inflow direction, and 'oblique' in this context means the vortices have an angle in the y-plane.

Different parts of the gap are referred to in terms of the different parts of the cylinder geometry. 'Vertical gap' refers to the gap between the straight vertical extensions, while 'curved gap' refers to the gap between the curved cylinder parts and 'horizontal gap' refers to the gap between the straight horizontal extensions.

Subscripts u and d refer to the upstream and downstream cylinders, respectively.

3. Results

3.1. *Overview of the flow topology*

The wake of curved tandem cylinders is very complex, owing to the spanwise variation of flow regimes, as well as the axial flow. Figure 4 shows the wake topology at two time instances. The basic tandem flow regime, which is found in the upper part of the flow domain, is alternating overshoot/reattachment. Further down, there is a gradual transition from reattachment to gap vortex shedding. The approximate location of gap shedding inception is marked in figure 4(*a*). Similar to single curved cylinders in the convex configuration, there is a clear von Kármán vortex street in the wake, and the spanwise vortices may be oblique, with a shedding angle α, or parallel, as depicted in the middle panels of figures 4(*a*) and 4(*b*), respectively.

Strong downdrafts in the lower gap and wake cause the vortices in these regions to have significant streamwise vorticity, a phenomenon which is clearly shown when the time-averaged vorticity is considered, depicted in figure 5. We see that, although the spanwise vorticity is stronger, the streamwise component cannot be neglected. This is also clear from figure 4, where the vortices in the lower gap and near wake align with the local curvature of the cylinders. Time-averaged fields, the extent of the recirculation region and the stagnation points of the vertical velocity will be further discussed in § 3.6.

In the upper wake, the spanwise vortices are bridged by counter-rotating streamwise vortex pairs, as shown in inset B of figure 4(*b*). The wavelength of the streamwise vortex pairs appears to be approximately one diameter; a topology reminiscent of the single cylinder three-dimensional instability mode B, described by Williamson (1996). However, if we consider the spanwise vortex undulations in figure 4(*b*), they seem to have a wavelength close to 4*D*. According to Carmo *et al.* (2010*a*), the three-dimensional instability for tandem cylinders at $L/D = 3.0$, $Re = 500$ is mode T3, with a spanwise wavelength of approximately 5*D*. This corresponds well with the wavelength of the spanwise vortices in figure 4(*b*). We believe that the short wavelength of the streamwise structures can be attributed to the large number of secondary vortices that arise from the interaction between the gap shear layers and near wake within the alternating reattachment/overshoot regime, previously described by Aasland *et al.* (2023) for the wake behind straight tandem cylinders.

Vortex dislocations occur frequently in the near wake, predominantly in the region $-4 \leq z/D \leq 0$, along the upper portion of the curved cylinder, but also in the lower wake, typically below $z/D = -6.5$. These regions represent generation of dislocations by means of two different mechanisms: in the upper region the dislocations stem from spanwise frequency differences, whereas in the lower region they occur due to gap vortex shedding. These dislocations will be referred to as type 1 and type 2, respectively. An example of a type 1 dislocation forming in the upper region of the near wake is shown in figure 4(*a*).

From figure 6, we see that the occurrence of a dislocation is often followed by others, so that time intervals of reasonably straight vortex lines are followed by intervals of comparable disorder. These events are related to flow mode variations in the gap, something which will be further discussed in § 3.3. Figure 6 also shows incidents where the two dislocation types occur nearly simultaneously.

The inherent three-dimensionality of the geometry enhances bending and tilting of the vortex cores in the wake, resulting in almost knitting-like patterns, especially in the lower part of the wake. Here, three-dimensionality is further strengthened by the interaction with the gap vortices (see inset C of figure 4*b*), as well by friction from the cylinder surface which causes retardation. Such a 'knitting pattern' is highlighted in inset A of figure 4(*a*),

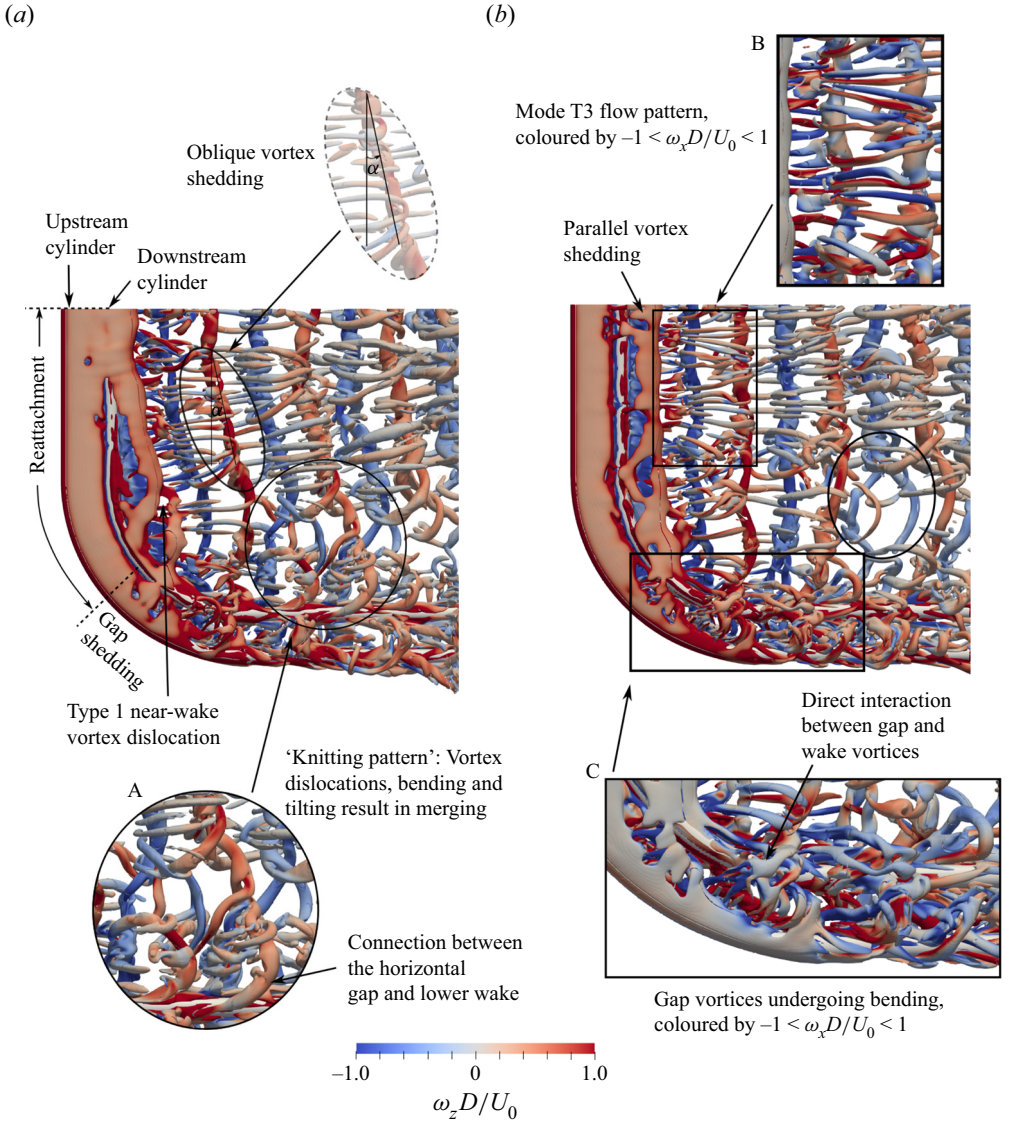

Figure 4. Instantaneous flow field, represented by isosurfaces of $Q(D/U_0)^2 = 0.02$ coloured by the vertical vorticity. Two distinct shedding modes are found in the wake: (*a*) oblique mode, at $tU_0/D = 850$ and (*b*) parallel mode, at $tU_0/D = 2450$. The vortex dynamics of the wake is extremely complex, due to vortex dislocations, bending, tilting and interaction between the structures in the lower wake and the horizontal gap. Dislocations are caused by two separate mechanisms, namely frequency differences (type 1, $-4 \leq z/D \leq 0$) and gap vortex shedding (type 2, $z/D \leq -6.5$).

where spanwise vortex dislocations, combined with bending and tilting of the streamwise vortices, results in merging of spanwise and streamwise structures.

Although the primary vortex shedding frequency persists unchanged along the entire gap, there are secondary frequencies, and these are particularly strong in the region $-4 \leq z/D \leq 0$ (a comprehensive spectral analysis is given in § 3.4). The resulting spanwise phase differences cause bending of the spanwise vortices which can be quite substantial. This is shown in figure 7(*a*), where massive bending of the vortices seems to propagate from the region near $z/D = -2$. The bending of the spanwise vortices causes rotation of

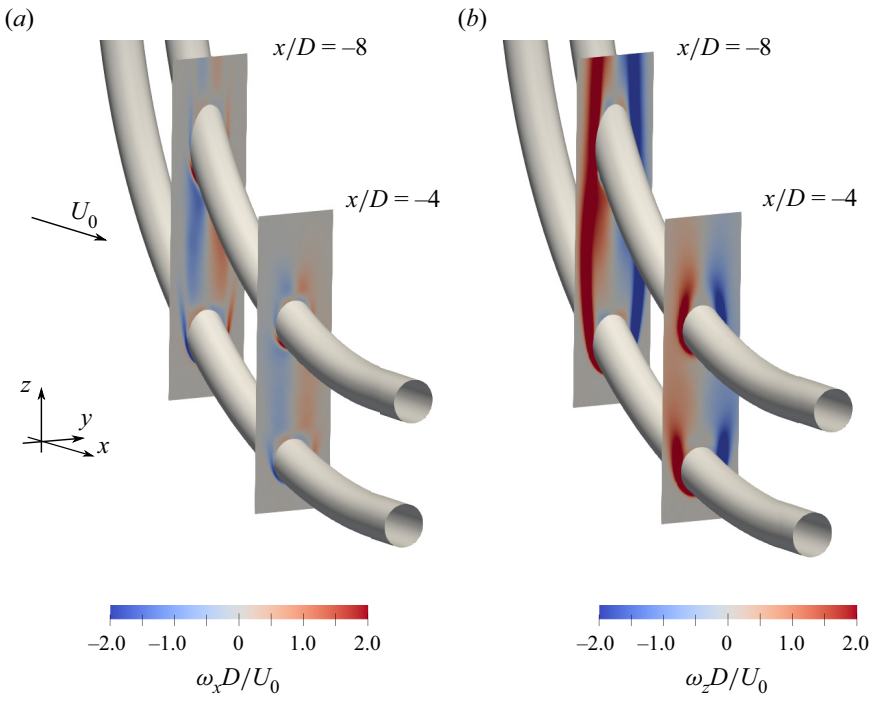

Figure 5. Time-averaged (*a*) streamwise and (*b*) spanwise vorticity in two planes in the lower gap and wake. It is clear from (*a*) that the vorticity of the gap vortices has a strong streamwise component due to the curvature-induced axial velocity.

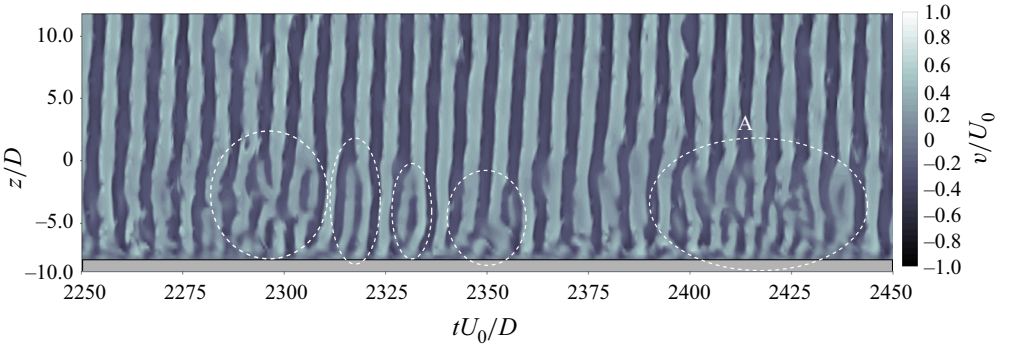

Figure 6. Temporal development of the cross-flow velocity along the probe line at $x/D = -4$, over an interval of 200 time units. The downstream cylinder is marked in grey. Spanwise vortex dislocations, marked by white dashed ovals, are frequent in the wake. During the event marked A, dislocations of both type 1 and type 2 occur simultaneously. This particular event can also be observed in figures 7(*a*) and 7(*b*).

the streamwise vortices in the braid region at an angle $\gamma \approx 16^\circ$ at the upper boundary. At the lower boundary, the angle is somewhat larger, due to the retardation of the vortices by the horizontal part of the downstream cylinder. This finding corresponds rather well to the results of Williamson (1992) for forced symmetrical dislocations at a Reynolds number of 300. Measured visually, the half-angle of the Λ-shaped dislocation was 12°, whereas using a definition based on the streamwise velocity fluctuations gave an angle of 18°. One must keep in mind, however, that in Williamson's (1992) study, dislocations occurred periodically, being forced, whereas in an unforced transitional wake they are intermittent.

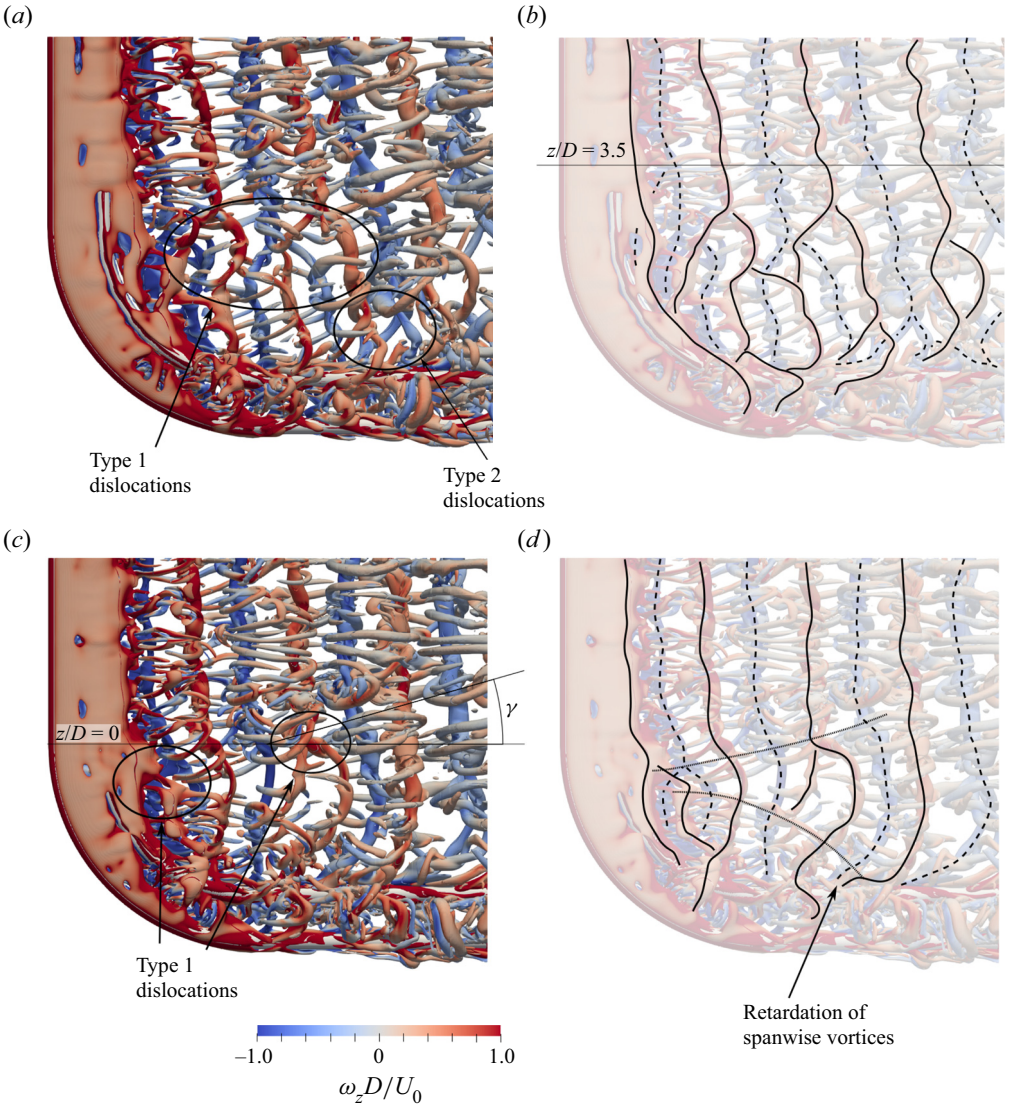

Figure 7. Instantaneous flow field at (*a*) $tU_0/D = 1250$ and (*c*) $tU_0/D = 3800$, represented by isosurfaces of $Q(D/U_0)^2 = 0.02$ coloured by the spanwise vorticity. In (*b*) and (*d*), solid lines trace vortex cores of positive spanwise vorticity, while vortex cores of negative spanwise vorticity are traced by dashed lines. In (*a*), both types of dislocations can be identified in the wake. Moreover, a type 1 dislocation occurs as high up as $z/D \approx 3.5$, easily seen in (*b*). Due to frequency and phase differences, as well as retardation due to the horizontal cylinder part, the spanwise vortices in (*d*) undergo massive bending in the y/D plane. This is highlighted by the vertically dashed lines. The bending of spanwise vortices leads to rotation of the streamwise vortices in the braid region. In the present snapshot, the rotation angle is $\gamma \approx 16^\circ$.

Both types of spanwise vortex dislocations identified in the present study can be observed in the wake of figure 7(*b*). This cluster of dislocations is in fact the same event which was captured some periods earlier by the probe line at $x/D = -4$, shown in figure 6. In the simplified figure 7(*b*), we see an uncharacteristic occurrence of a spanwise vortex dislocation along the straight vertical extension, near $z/D = 3.5$. Supplementary material and movie 1, available at https://doi.org/10.1017/jfm.2023.933, illustrate the development of dislocations in the lower wake.

3.2. *Spanwise development of flow regimes*

The spanwise variation of flow regimes is visualised in figure 8. The flow pattern changes gradually from alternating overshoot/reattachment (figure 8*a–c*), to stable reattachment (figure 8*d*,*e*), until vortex shedding finally commences in the gap (starting from figure 8*f*).

Compared with the wake at $z/D = 5$ in figure 8(*a*), the wake at $z/D = 2$ and $z/D = 0$ (shown in figures 8(*c*) and 8(*d*), respectively) is intricate. This region, which is located directly below the rectangle which marks inset B in figure 4(*b*), features significant bending and tilting of streamwise eddies, so that these gain a clear spanwise vorticity component, resulting in clusters of secondary vortices in the planes $z/D = 2$ and $z/D = 0$.

The small wake vortex observed in figures 8(*d*) and 8(*e*) is one leg of a spanwise vortex dislocation, marked by an oval in figure 4(*b*). In fact, this particular vortex exhibits both type 1 and type 2 dislocations (see figure 7*a*). The small vortex cluster in figure 8(*e*) consists of two vortices twisting around each other in a helical manner. Higher up, in figure 8(*d*), they have paired.

In figure 8(*f*), the flow is bi-stable with one-sided reattachment, meaning that vortices are repeatedly shed from a single shear layer, while the opposite shear layer reattaches. Some of these vortices are marked in figure 8(*f*). Far downstream it becomes increasingly hard to distinguish gap vortices from other vortical structures in the lower wake. In the case of straight tandem cylinders, a so-called binary vortex street is formed for gap ratios between the critical spacing and $L/D = 6$ (Zdravkovich 1987). Here, vortices from the upstream cylinder are convected downstream alongside downstream cylinder vortices of the same vorticity sign, without merging. From figure 8(*f*), the wake can be described as loosely binary (on one side), although the gap and wake vortices are staggered. However, one must keep in mind the three-dimensionality of the flow. The gap vortices in the lower wake form the legs of type 2 dislocations.

Near-wake vortex shedding persists down to approximately $z/D = -8$, as seen in figure 8(*g*). Here, the axial flow has grown strong enough to partially inhibit communication between the shear layers, and true shedding only occurs intermittently. A mere $0.5D$ lower, in figure 8(*h*), there is no longer vortex shedding in the near wake. The gradual change from von Kármán shedding to non-shedding causes narrowing of the wake width, so that the spanwise vortices have a slight inclination away from the symmetry plane. It is worth noting that, from a statistical point of view, near-wake vortex shedding is suppressed already at $z/D = -6$, an observation which is discussed in § 3.6. However, there are large temporal variations.

The character of the vortex formation in the gap gradually changes between $z/D = -7$ and -9.5 (figures 8*f* and 8*i*, respectively), as both the effective gap ratio and the vertical velocity increase. Reattachment occurs intermittently at both $z/D = -7$ and -8, something which will shortly be discussed in some detail, while further down, the vortices of both gap shear layers undergo complete roll up. The formation length of the vortices shortens as the gap ratio increases, so that at $z/D = -9.5$ a short wake is formed in the gap. The strong axial flow imposes additional stress and strain on the gap vortices in this region, which accelerates the transition to turbulence and hastens vortex breakdown, as seen in figure 8(*i*). With increased vertical velocity comes an increase of small secondary eddies in the gap, as vorticity is transferred from the large-scale gap vortices. This is seen in figures 8(*g*) and 8(*h*).

In the horizontal gap, the structure of the vortices is extremely complex. In figure 8(*j*), we see that a vortex street forms in the wake of the upstream cylinder, which features a

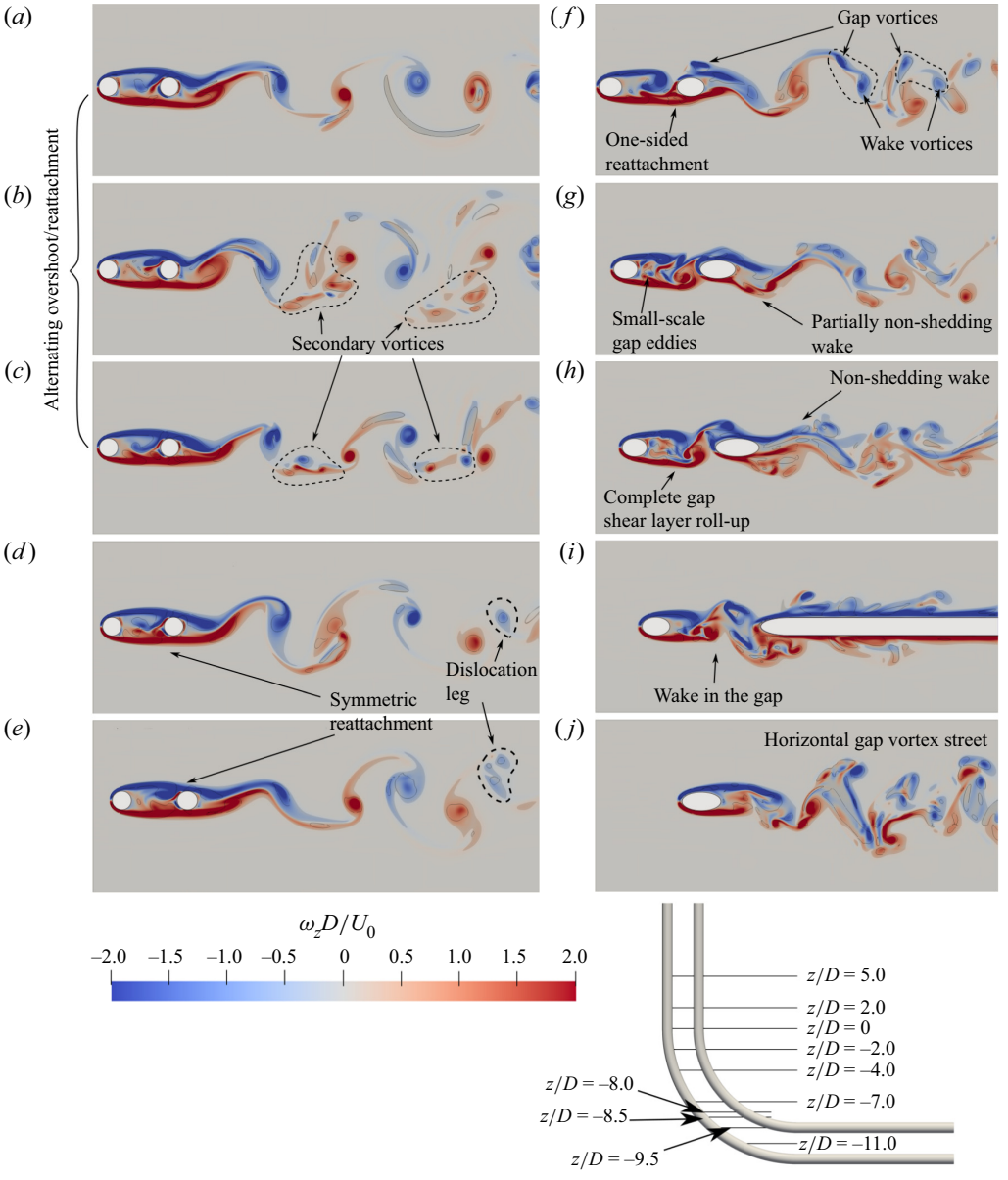

Figure 8. Spanwise development of the instantaneous wake flow at $tU_0/D = 2450$, represented by vertical vorticity and contours of $Q(D/U_0)^2 = 0.1$. Along the straight vertical extension, (*a–c*), there is alternating overshoot/reattachment. The flow regime changes to symmetric reattachment between $z/D = 0$ and -2, (*c*) and (*d*), respectively. Symmetric reattachment persists in (*e*). Panel (*f*) shows a one-sided bi-stable regime where gap and wake vortices form staggered pairs (marked by dashed lines). Vortices are shed from both sides of the gap in (*g*), though communication between the shear layers is still partly inhibited. Depending on the flow mode, shedding may occur in the near wake. In (*h*) there is complete roll-up of the gap vortices, but the axial flow prevents vortex shedding in the near wake. A wake forms in the gap in (*i*). Panel (*j*) shows the vortex street in the horizontal part of the gap. Along the curved part, the effective gap spacing L_e has been computed by measuring the spacing from the upstream cylinder back to the downstream cylinder front and adding $1D$. (*a*) $z/D = 5.0$, $L/D = 3.0$, (*b*) $z/D = 2.0$, $L/D = 3.0$, (*c*) $z/D = 0$, $L/D = 3.0$, (*d*) $z/D = -2.0$, $L_e/D = 3.2$, (*e*) $z/D = -4.0$, $L_e/D = 3.6$, (*f*) $z/D = -7.0$, $L_e/D = 4.2$, (*g*) $z/D = -8.0$, $L_e/D = 4.6$, (*h*) $z/D = -8.5$, $L_e/D = 4.8$, (*i*) $z/D = -9.5$, $L_e/D = 6.1$ and (*j*) $z/D = -11.0$.

large number of secondary structures. This wake is in fact wider than the lower wake of the downstream cylinder. This is because the vortices in the horizontal gap loop outwards, away from the symmetry plane, as seen in figure 4(*b*).

In the present study, it is not just the effective gap ratio that changes along the span, but also the cross-sectional shape of the cylinders in the z/D planes. For a straight inclined cylinder, it is first and foremost the axial velocity that influences the shedding regime, not the local cross-sectional shape (Shirakashi, Hasegawa & Wakiya 1986). Meanwhile, the case of curved tandem cylinders is more complex, due to the fact that the cross-sectional shape of the downstream cylinder influences the interaction between the gap and wake flows.

Because the upstream and downstream cylinders have different radii of curvature, their cross-sections do not change at the same rate. The change is much faster in the downstream cylinder, with a lower r_c resulting in a configuration with a slightly elliptical cylinder upstream and an increasingly elongated cross-section downstream (see figures 8*f*–8*h*). This occurs within the gap shedding region, and has two different implications: (i) an elongated downstream body gives the structures from the upstream shear layer more time to interact with the downstream cylinder boundary layer, (ii) vortices shed in the gap impinge at different locations than they would have on a circular downstream cylinder cross-section. One example is the staggered binary vortex pairs in figure 8(*f*).

3.3. *Flow bi-stability*

In the present study, the flow is bi-stable. It is important to note that this does not merely encompass the switch between reattachment and shedding which occurs in the lower gap; bi-stability is present along the entire span, including the region of alternating overshoot/reattachment. This is consistent with the results of Aasland *et al.* (2023), who showed that there are two flow modes in the gap and near wake of straight tandem cylinders at $L/D = 3$ and $Re = 500$.

Within the reattachment region, the second flow mode generally manifests itself in stronger vortex interactions, stronger velocity fluctuations and wider widths of the gap and wake. Moreover, gap shear layer overshoot penetrates further into the near wake. In accordance with Aasland *et al.* (2023), the second mode may manifest locally, but in the present case the axial velocity enhances communication along the span, and this may trigger a switch of flow modes at additional spanwise locations. In the supplementary material and movie 2, the mode switch first occurs at $z/D = 0$, subsequently at $z/D = -6$ and then finally at $z/D = -8$. The second mode is associated with increased vertical velocity fluctuations. While the time-averaged vertical velocity at $z/D = 0$ is positive (see figure 17), strong gap vortices have a significant streamwise vorticity component even at this z/D level. Second mode time intervals correspond to an increase in the number of dislocations of both types, such as the event depicted in figure 7(*d*).

In the lower gap, the switch between modes is similar to the prevailing understanding of tandem cylinder bi-stability, namely a switch between reattachment and true vortex shedding in the gap. This is exemplified in figure 9, for $z/D = -8$. Here, periods of relatively calm flow, with mostly reattachment or one-sided reattachment, are followed by periods of chaotic flow with shedding from both gap shear layers and strong interaction with the near wake. The downstream cylinder shear layer oscillations increase during intervals of the second mode, and may precipitate intermittent near-wake vortex shedding at $z/D = -8$.

The time instances shown in figure 9 are chosen to highlight some typical features of the temporal development of the lower gap flow. Figures 9(*a*)–9(*e*) are part of an interval

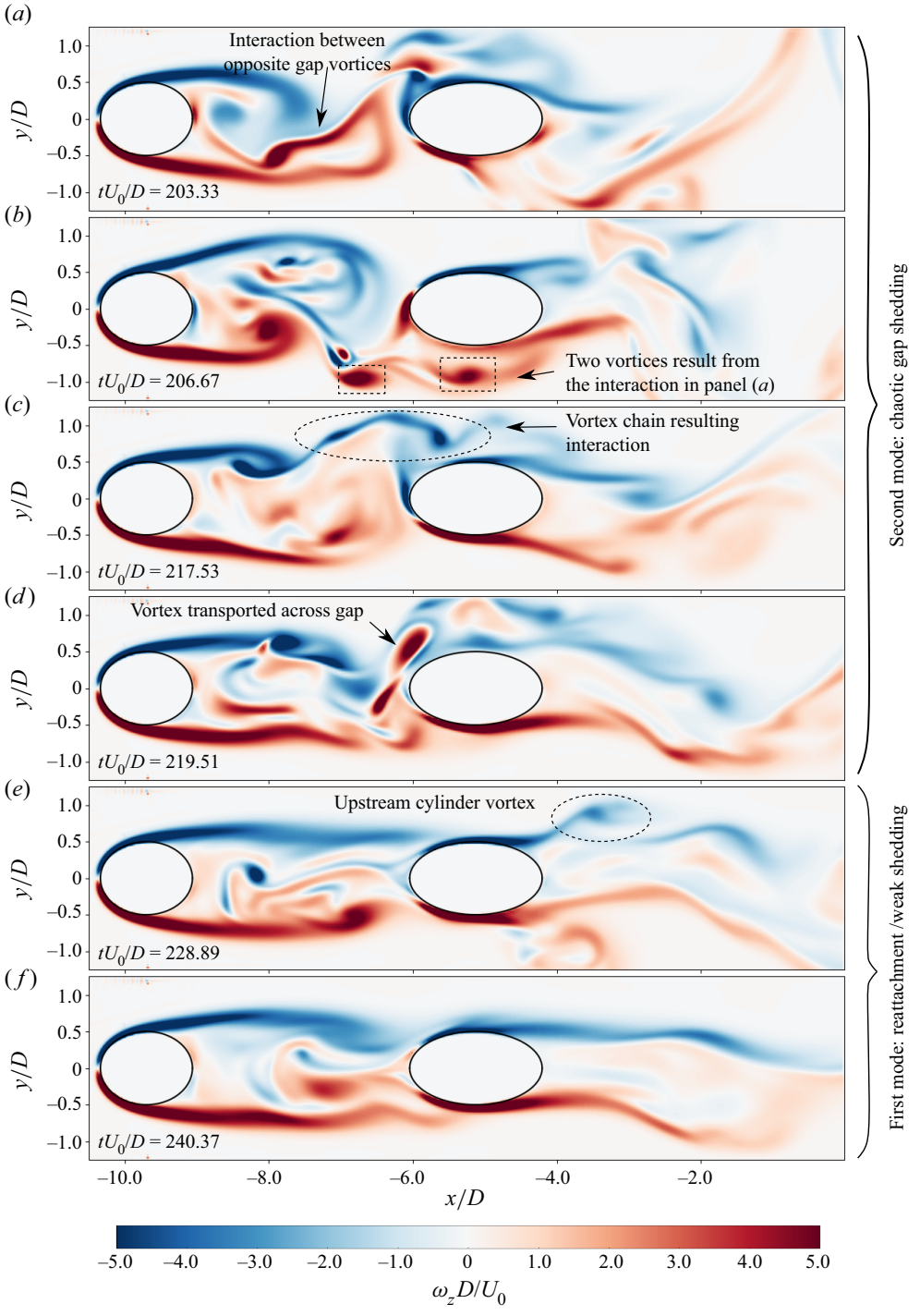

Figure 9. Selected time instances of the flow in the plane $z/D = -8$, represented by vertical vorticity. Panels (*a–d*) depict a chaotic period of strong gap shedding. In panel (*e*), this period is coming to a close, with the flow returning to a state of variation between weak gap shedding and reattachment. In panel (*f*), the flow is in the middle of a calm period.

of chaotic gap shedding which lasts for some 30 time units, corresponding to roughly 5 large-scale vortex shedding periods. In figure 9(*a*), the large-scale vortex forming in the upper shear layer interferes with the vortex that has recently formed in the lower shear layer (event marked by black arrow). Instead of being cleanly shed, this vortex is cut into two separate, smaller vortices, marked by dashed rectangles in figure 9(*b*). A similar event occurs later in the chaotic interval, resulting in a chain of smaller vortices, this time in the upper shear layer, as seen in figure 9(*c*) (dashed oval). Moreover, the interaction between the gap shear layers results in the formation of structures of opposite rotation which are sucked into the flow passed the upper side of the downstream cylinder (black arrow in figure 9*d*). Figure 9(*e*) depicts a much calmer flow, towards the end of the chaotic time interval, and in figure 9(*f*), the flow is back to weak gap shedding interspersed with reattachment. Note that the vortex in the upper shear layer of the downstream cylinder figure 9(*e*) (dashed oval) originates from the upstream cylinder.

3.4. *Spectral analysis*

Spectra of the cross-flow velocity, computed from probe time traces, are shown in figure 10. The spectral peaks in the present study reproduce those of Aasland *et al.* (2023), where the dominant frequency is $fD/U_0 = 0.143$, with secondary peaks of $fD/U_0 = 0.147$ and 0.155. This is clearly shown in inset G, in the lower right of figure 10. The secondary peaks are connected to the mode switch phenomena described in § 3.3, and their relative importance grows in the lower gap and wake, as mode switches become more frequent.

Not only are the dominant and secondary frequencies the same as for straight tandem cylinders; their value also remains nearly constant along the gap and wake. From single curved cylinder studies in the literature, we know that the vortex shedding in the lower wake is largely governed by the frequency of the shedding in the upper wake (Miliou *et al.* 2007; Gallardo *et al.* 2014). The same appears to be true for tandem curved cylinders, where the vortices along the straight vertical extension govern the frequencies in the rest of the flow.

The degree to which the vortices in the upper part of the gap and wake dominate the Strouhal number likely depends on the length of the straight vertical extension. A longer length favours strong vortices with an orientation normal to the inflow direction. Moreover, the fact that the dominant frequencies are near identical to those in the straight tandem cylinder case indicates that the parallel vortex shedding is more common than oblique shedding.

In the wake, there are two secondary broadband peaks, centred approximately on $fD/U_0 = 0.18$ and 0.23. These peaks are not present to any significant degree along the straight vertical extension, but are well defined in the region $-4 \leq z/D \leq 0$. The peaks are caused by vortex dislocations of type 1, which occur frequently in this spanwise region. If we consider figure 6, we see that a point probe in the wake located for instance at $z/D = -3$ is passed by a larger number of vortex cores during the given time interval than a probe higher up in the wake.

Wavelet analysis of the cross-flow velocity confirms the existence of rather long intervals of dislocations (such as event A in figure 6). From the spectral map in figure 11, we see that f_v does not necessarily co-exist in time with the secondary peaks. In inset A of figure 11, the secondary frequencies dominate f_v over an interval of some 130 time units. This is quite a long time, considering that it covers 18 vortex shedding cycles, using f_v as a reference. Most of the intervals are shorter than the one shown in inset A, however. The typical duration of these dislocation intervals seems to correspond well to the observed lifetime

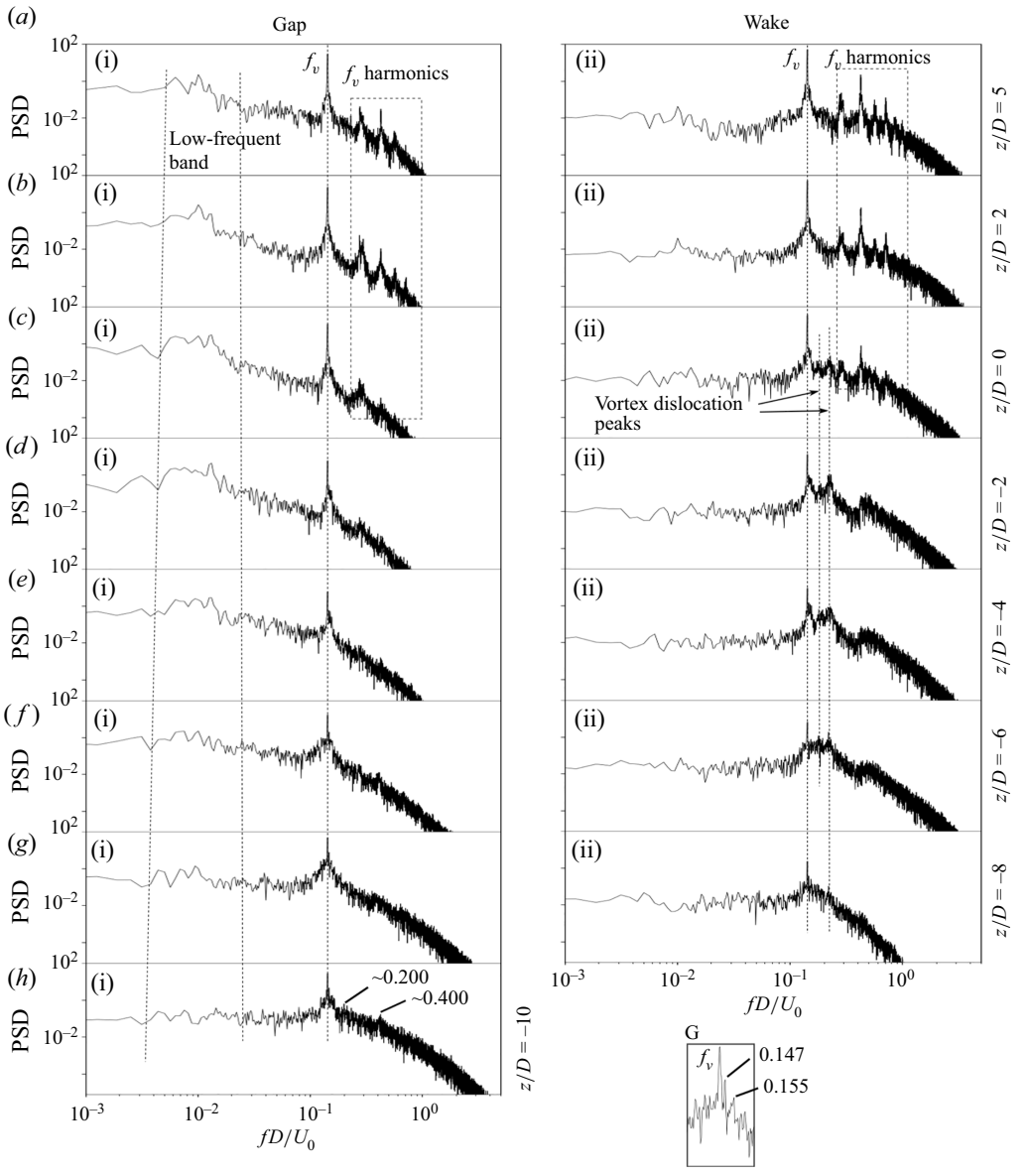

Figure 10. Cross-flow velocity spectra taken at $y/D = 0.0$, at various z/D locations in the gap and wake (probes PG1–8 and PW1–7, see figure 3*d*). Inset G shows a close up of the spectral peaks in (*g*). The secondary peaks occur owing to the flow bi-stability. There is significant low-frequency content, and its power spectral density (PSD) is highest in the gap.

of the mode switches described in § 3.3, which underlines the connection between these two phenomena.

There is significant low-frequency activity in the flow, which is clearly shown in the cross-flow velocity spectra of figure 10. The low frequencies appear in a broad band, but there are also distinct spectral peaks within this band. The energy of the low-frequency spectral band is significantly higher in the gap than in the wake. If we look at figure 10(*a–h*), we see that there is a gradual shift towards lower frequencies as we

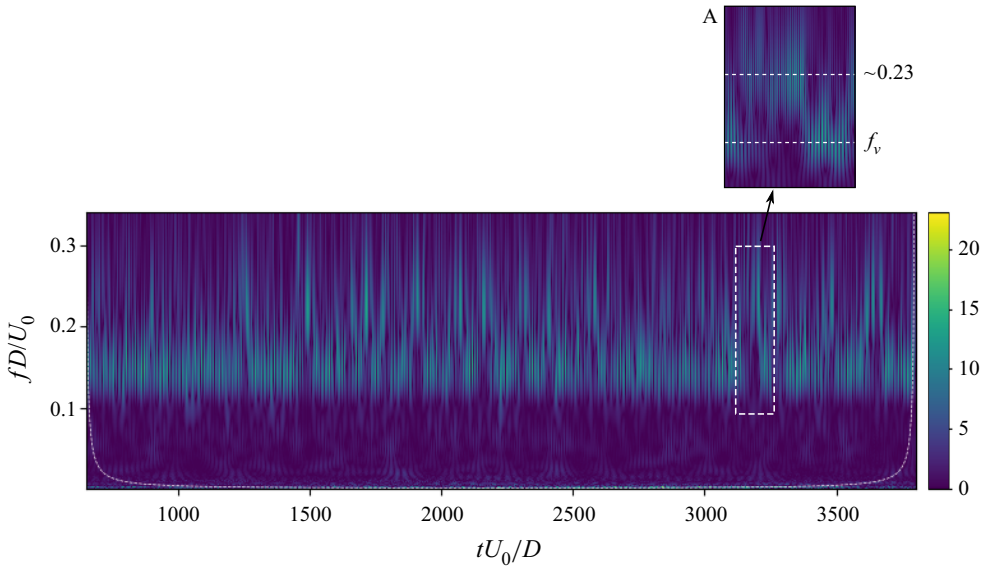

Figure 11. Wavelet map of the cross-flow velocity at wake probe PW3. The corresponding spectrum is shown in figure 10(*d*ii). During certain time intervals, the higher frequency peaks seen in the spectrum become significantly stronger than f_v, as seen in inset A. The inset covers the time interval $3130 \leq tU_0/D \leq 3260$, which corresponds to around 18 cycles of f_v. The broken lines mark the cone of influence.

move downwards in the gap, while the overall spectral energy within the band decreases somewhat.

The *in situ* FFT analysis shows that, for the lowest analysed frequency, $fD/U_0 = 0.0089$, the spectral content is mainly concentrated in the lower part of the curved gap, as depicted in figure 12(*a*). However, there is also significant spectral energy associated with the gap shear layers and gap vortices at higher z/D, as seen in figures 12(*b*) and 12(*c*). The same holds true for for $fD/U_0 = 0.0178$ and 0.0356, but only the lowest frequency is shown herein, for brevity.

Within the gap shedding region, in figure 12(*e*), we see that the highest spectral energy of $fD/U_0 = 0.0089$ seems to be clustered near the cores of the swirling gap vortices. There is a second type of cluster along the gap centreline, which is located upstream of the gap vortices. This is connected to long-term variation of the axial flow.

At $z/D = -8$, shown in figure 12(*d*), the spectral energy cluster is located around the streamwise extent of the vortex formation region, but it is distinctly asymmetrical. The frequency $fD/U_0 = 0.0089$ was captured during the second set of *in situ* FFT analyses, which only ran for 150 time units. Thus, only a single period of this very low frequency was analysed. However, this result indicates that there may be cross-flow meandering of the vortex formation region whose frequency is too low to appear in the visualisations.

At the probe shown in figure 10(*h*), which is located nearly in the horizontal part of the gap, the downstream cylinder is no longer directly in the wake of the upstream cylinder; the geometrical constraints are now above and below. Moreover, the local cross-section is no longer circular; it is elliptical with an aspect ratio of approximately $AR = 0.47$, where AR is defined as the ratio between the minor (y-direction) and major (x-direction) axes of the ellipsis.

The frequencies are still dominated by vortices along the straight vertical extension. However, figure 10(*h*) shows a broad-banded secondary peak, centred on $fD/U_0 = 0.200$, and its harmonic $fD/U_0 = 0.400$. This frequency is not significant higher up in the gap.

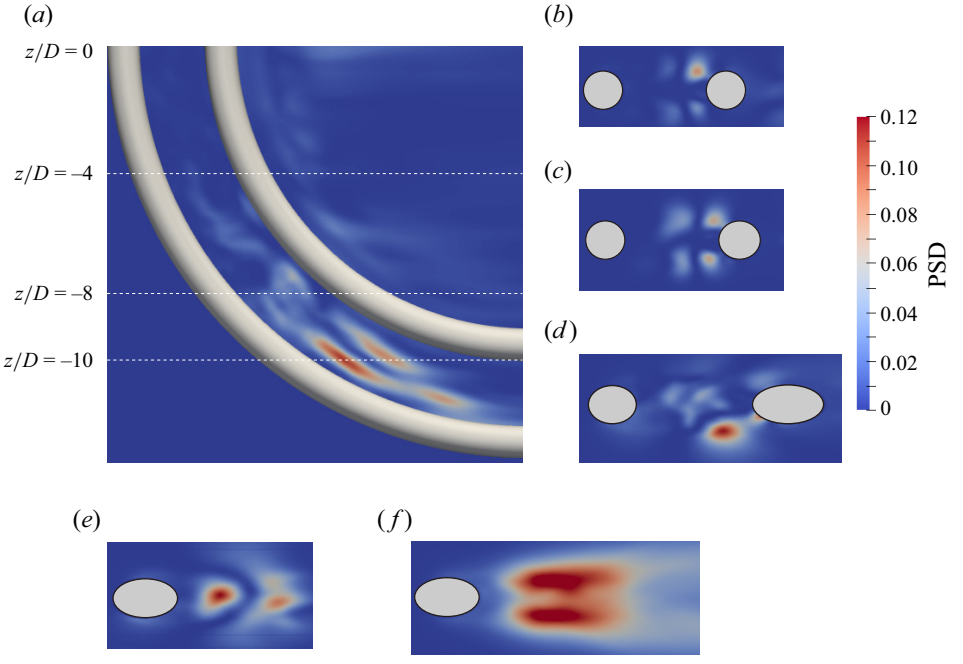

Figure 12. (*a–e*) Spectral map of the frequency $fD/U_0 = 0.0089$. The energy of this low frequency is mainly concentrated in the lower part of the curved gap, in the vortex formation region of the upstream cylinder, but it is also significant for the formation of gap vortices in the upper part of the curved gap. (*f*) Spectral map of $fD/U_0 = 0.2175$. This frequency is part of a broad-banded spectral peak centred around $fD/U_0 = 0.20$. In (*d*), the asymmetry with respect to the gap centreline is a result of the short sampling period. Panels show (*a*) $y/D = 0$, (*b*) $z/D = 0$, (*c*) $z/D = -4$, (*d*) $z/D = -8$, (*e*) $z/D = -10$ and (*f*) $z/D = -10$.

The *in situ* FFT analysis has captured a spectral map of $fD/U_0 = 0.2175$, shown in figure 12(*f*), which is part of the broad-banded peak. In the figure we see that the spectral energy is primarily clustered in the shear layers of the upstream cylinder, in the formation region of the swirling vortices. This indicates that the formation length varies. We believe the broad-banded peak may result from a mode switch where the most unstable mode represents a flow similar to a single bluff body wake, in this case an elliptical cylinder.

A wavelet map of the cross-flow velocity in the probe from figure 10(*h*), along with all three velocity components, is shown in figure 13. In figure 13(*c*), we see that the cross-flow velocity time trace is quasi-periodic, consisting of relatively high-amplitude intervals interspersed with irregular intervals of low-amplitude fluctuations. Comparing the time trace with the wavelet map, we see that the irregular intervals correspond to a downward shift of the dominant frequency. An upward shift of the dominant frequency, towards $fD/U_0 \approx 0.2$, accompanies intervals of stronger, more regular velocity fluctuations, which is indicative of a shorter vortex formation length. Intuitively, a shorter formation length in this part of the gap allows increased flow along the downstream cylinder front face, and figure 13(*a*) shows that strong cross-flow and vertical velocity fluctuations are accompanied by an increase of the streamwise velocity (u/U_0 is predominantly positive in this part of the gap).

Though we cannot conclude firmly with the available data, the high-frequency intervals are believed to represent the 'single bluff body' mode suggested above. It would have been beneficial to compare the frequency of the broad-banded peak with the dominant frequency of an elliptical cylinder. Regrettably, we have found no studies of elliptical

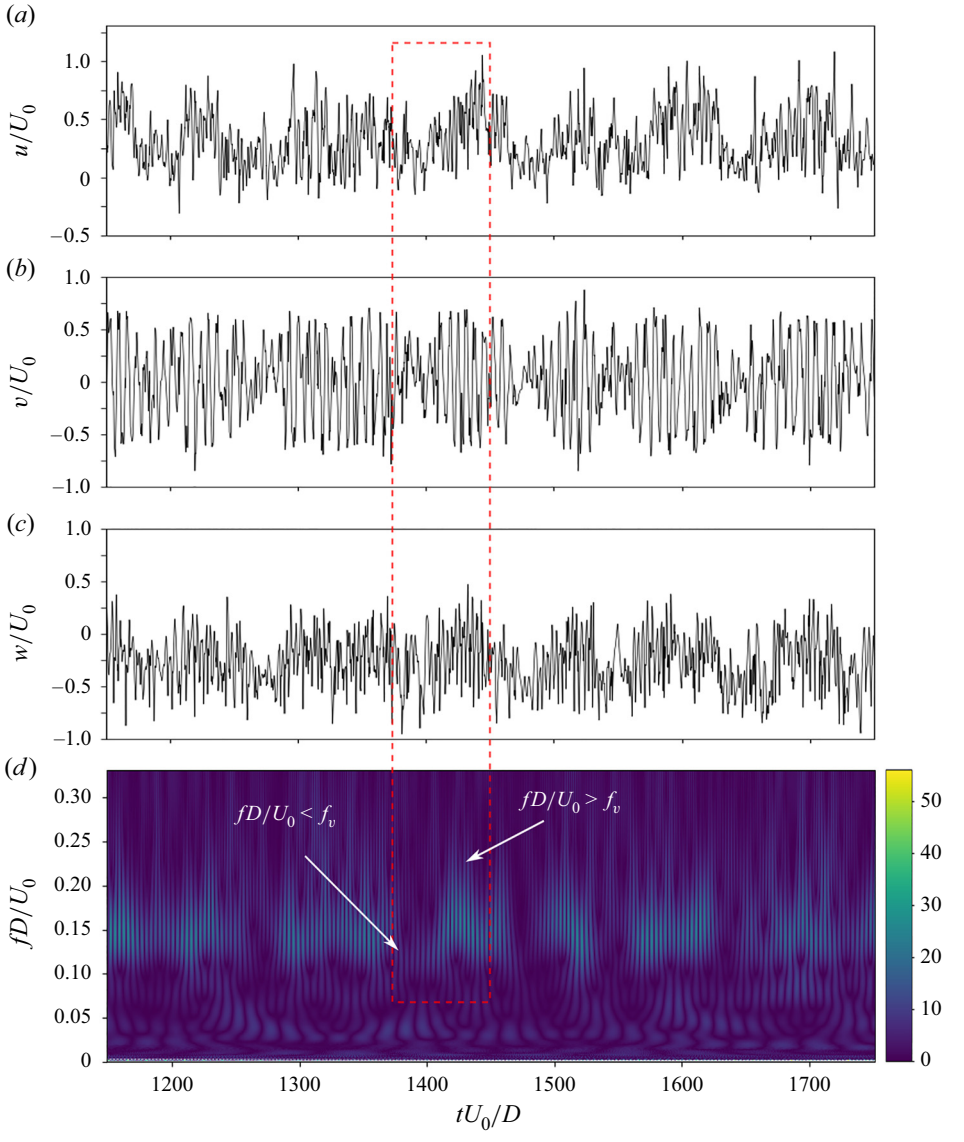

Figure 13. (*a*) Streamwise, (*b*) cross-flow and (*c*) vertical velocity time traces, as well as (*d*) the cross-flow velocity wavelet map at probe PG8, in the lower curved gap. Intervals of irregular low-amplitude velocity fluctuations correspond to a lowering of the dominant frequency. Conversely, high-amplitude fluctuations correspond with an increase in the dominant frequency. The spectrum at this probe is shown in figure 10(*h*).

cylinders with comparable conditions that report *St*. A study with a Reynolds number of 150 found $St \approx 0.17$ for $AR = 0.5$ (Shi, Alam & Bai 2020), but at such a low *Re* the flow is two-dimensional.

3.5. *Low-frequency quasi-periodic gap asymmetry*

In the upper part of the gap (above $z/D \approx -2$), vortices are often shed repeatedly from one shear layer. This long-term asymmetry results in an asymmetry of the transverse position

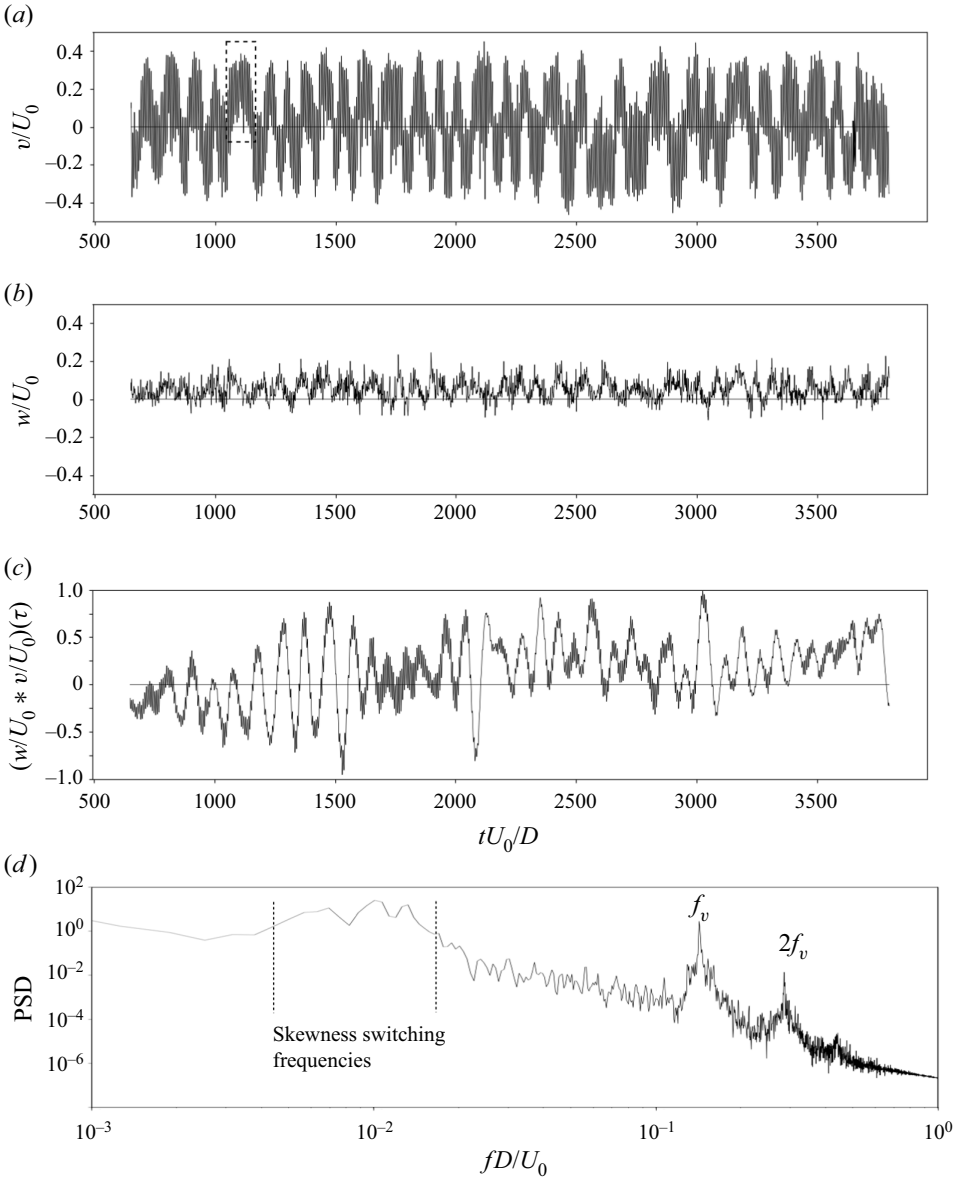

Figure 14. Time traces of (*a*) cross-flow and (*b*) vertical velocities at probe PG3 in the gap, at the intersection between the curved and straight cylinder parts. (*c*) Shows the cross-correlation between the velocities, and (*d*) shows the spectrum of the cross-correlation. The cross-flow is skewed with respect to the $v/U_0 = 0$ line, for long periods of time. In the dashed rectangle, for example, it is positive for several vortex shedding periods. Here, v and w are clearly correlated, and a switch in the skewness across the $v/U_0 = 0$ line is normally accompanied by a surge in $|w/U_0|$.

of the gap backflow region, which meanders on a time scale longer than that of the wake shedding. These results are consistent with the study of Aasland *et al.* (2023) on straight tandem cylinders, who showed that the asymmetry was caused by a mode switch in one shear layer. In that study, the mode switch occurred intermittently, while in the present study, the mode switch occurs quasi-periodically, so that the long-term asymmetry moves

between gap shear layers with a period of approximately 100 time units. This is clearly shown in figure 14(*a*), which shows the cross-flow time trace of a probe in the gap, at the intersection between the straight vertical extensions and curved cylinders. Although the long-term average may be zero, the cross-flow velocity is skewed to either side of the $v/U_0 = 0$ line during several vortex shedding periods at a time. The temporal evolution of the flow field is exemplified in supplementary material and movie 3.

In figure 14(*b*), the vertical velocity is plotted. Close inspection reveals that a switch of the asymmetry is normally accompanied by a surge of $|w/U_0|$. The cross-flow and vertical velocities are clearly correlated, as shown in figure 14(*c*). Running an FFT of the cross-correlation produces a triple low-frequency spectral peak centred around $fD/U_0 = 0.01$, with secondary peaks at $fD/U_0 = 0.0065$ and 0.013, shown in figure 14(*d*). This frequency range corresponds well with the low-frequency band observed in the spectra in figures 10(*a*)–10(*g*), particularly within the reattachment region of the gap (i.e. above $z/D \approx -6$).

Behaviour similar to that of the time trace in figure 14(*a*) is found to a certain degree in the cross-flow velocity for all probes above $z/D = -4$ (shown for $-2 \leq z/D \leq 1$ in figure 15). However, the transverse switch is most clearly defined in the range $-4.0 \leq z/D \leq 0$. This is the range within which the bi-stability frequencies are most pronounced, as shown in the spectra of figures 10(*c*)–10(*e*), and also the range within which type 1 dislocations most frequently develop.

Figure 15 shows that the transverse switch is slightly out of phase along the span. It occurs first in the upper curved gap, and propagates upwards along the straight vertical extension.

3.6. *Recirculation and secondary flows*

In the time-averaged sense, the larger part of the gap region falls under the reattachment regime, which persists along the entire vertical extension and down to gap shedding angle, $\beta_{GS} = 38.1^\circ$, as shown in figure 16(*a*). The following gap recirculation bubble is suppressed at $\beta_{ru} = 45.6^\circ$. In comparison, recirculation in the wake is suppressed at $\beta_{rd} = 37.4^\circ$. These values are based on the time-averaged flow in the centreplane, and do not take the swirling vortices in the lower gap into account. The extent of the swirling vortices is shown in figure 18, which plots the zero shear stress contour on the cylinder surfaces. Their inception corresponds with the recirculation suppression.

The non-zero values of cross-flow velocity in the centreplane (figure 16*b*) are caused primarily by the long-term asymmetry of the gap vortices. The values are small compared with the straight tandem cylinder case of (Aasland *et al.* 2023). Long-term asymmetry is not confined to the reattachment region, with non-zero values of V/U_0 also appearing in the lower gap. This is consistent with the it in situ FFT results shown in figure 12(*d*).

In figure 16(*c*), we see that there is upwelling in the entire part of the vertical gap and near wake, which penetrates down to the stagnation points at $\beta_{stgu} = 44.7^\circ$ and $\beta_{stgd} = 34.3^\circ$, respectively. The upwelling velocities are low compared with the downdraft in the lower gap and wake, something which is clearly shown in figure 17. In both the gap and the wake, the stagnation points are located slightly higher than the point of suppressed recirculation. In the present study, the region of maximum upwelling velocity is found along the straight vertical extension, near $z/D = 2$. This differs from the single curved cylinder case of Gallardo *et al.* (2014), where the maximum upwelling velocities were found along the curved part of the cylinder, in the region that corresponds to $-6 \leq z/D \leq -2$ in the present study.

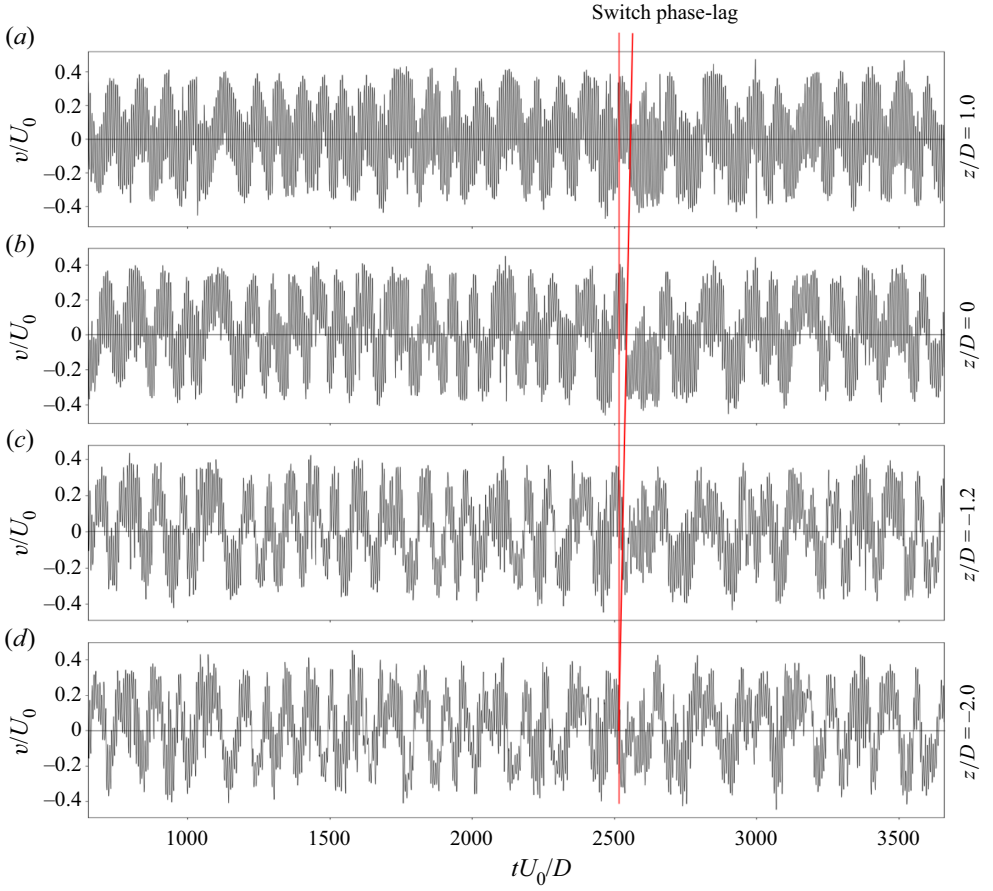

Figure 15. Time traces of cross-flow velocity at various z/D locations along the gap (probes PG10, PG3, PG9 and PG4). The quasi-periodic asymmetry switch in the gap is slightly out of phase along the span, as indicated by the red lines, with the switch first occurring in upper curved gap, then propagating upwards along the straight vertical extension.

There is a second upwelling zone in the wake, marked in figure 16(*c*), which spreads from the lower part of the vertical extension with a wedge-like shape. In this region, there is significant bending and helical twisting of the vortices, associated with the spanwise vortex dislocations. For a straight vortex tube, the induced velocity is purely circumferential, but when two vortices twist around each other in a helical manner (which happens when the dislocations legs join together), the induced velocity has a component along the vortex core axis (see figure 25 of Williamson 1992). Note that the upper boundary of the upwelling region has approximately the same angle as the rotated streamwise vortices of figure 7.

In figure 16(*a*), the contours in the near wake show that the streamwise extension of the recirculation bubble is considerably longer along the curved part of the downstream cylinder than along the straight vertical extension. This is quite different from the turbulent wake behind a single curved cylinder studied by Gallardo *et al.* (2014), where the recirculation bubble has approximately the same streamwise length down to the region of swirling flow, where it is gradually attenuated. The increase in recirculation length actually starts along the lower part of the straight vertical extension, near $z/D = 1$. It is also worth noting that the strongest backflow velocities are found in the region $-4 \leq z/D \leq 0$, which is also where the recirculation length is at its longest. The backflow velocities along the

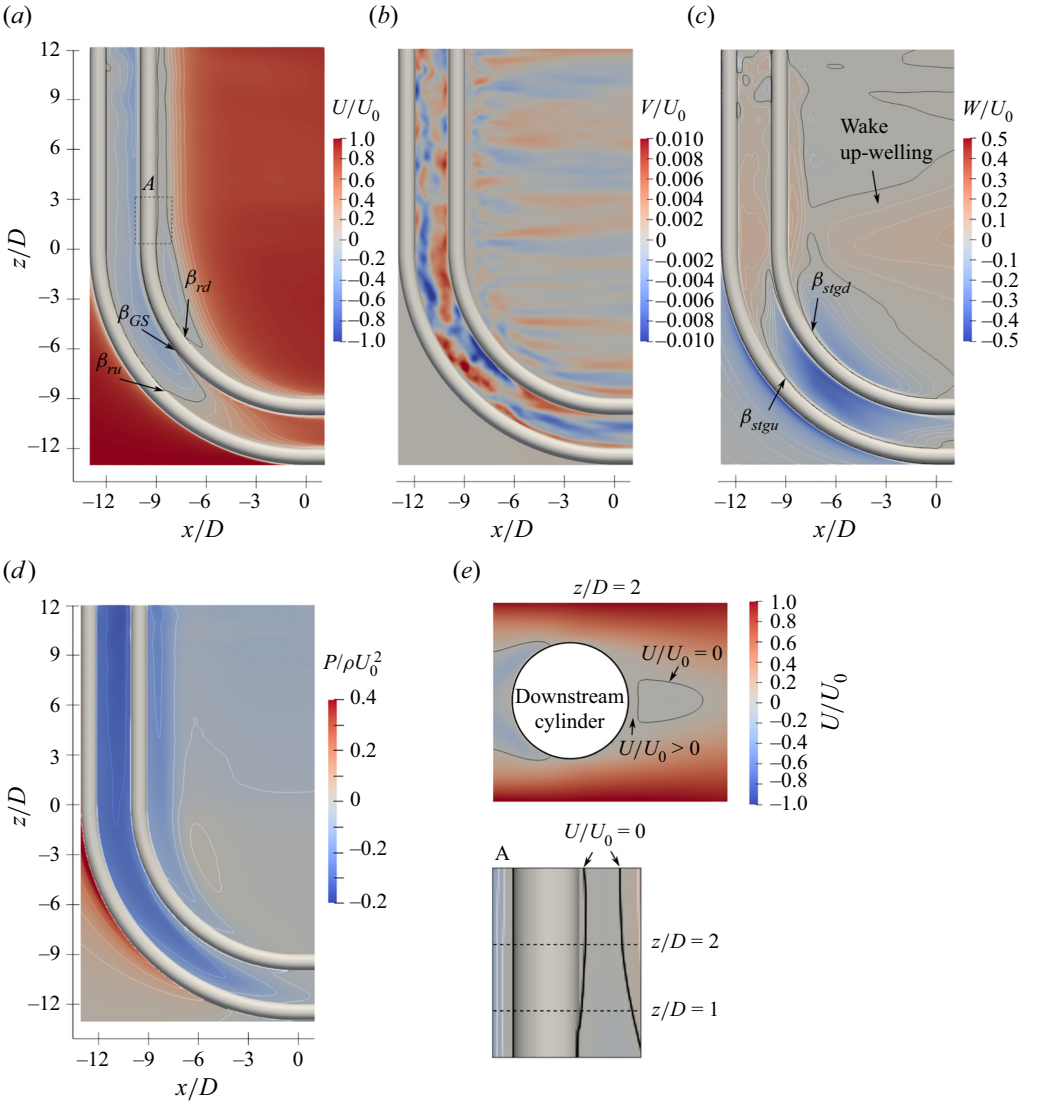

Figure 16. Time-averaged (*a*) streamwise, cross-flow and (*c*) vertical velocity, as well as (*d*) pressure in the symmetry plane. Black contour lines mark $U/U_0 = 0$ and $W/U_0 = 0$ in (*a*) and (*c*), respectively. (*e*) Shows the time-averaged streamwise velocity around the downstream cylinder in the plane $z/D = 2.0$. The contour $U/U_0 = 0$, shows that the recirculation bubble in the downstream cylinder wake is displaced by a region of low, positive streamwise velocities. Inset A, taken from (*a*), shows a close-up of the downstream cylinder in the region where this displacement starts.

straight vertical extension are low in comparison. This is different from the gap, where the strength of the backflow is nearly evenly distributed along the length of the reattachment region. This result is also in opposition to that of Gallardo *et al.* (2014), where the backflow is strongest along the straight vertical extension.

If we consider the pressure distribution in the symmetry plane, shown in figure 16(*d*), we see that the suction in the near wake is strongest along the straight vertical extension. It is well known that lowering the base pressure results in a shorter recirculation length (Gerrard 1966). Previously, it was found that, for straight tandem cylinders, the base

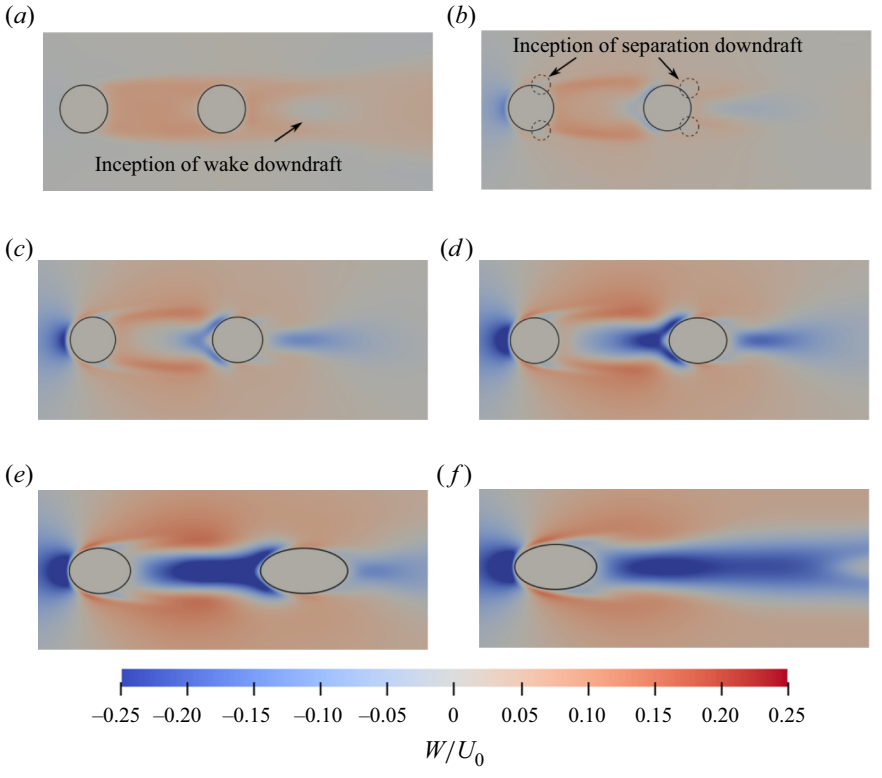

Figure 17. Time-averaged vertical velocity in various z/D planes. In the gap, downdraft along the downstream cylinder front face begins near $z/D = -1.5$ (see figure 16*c*). Along the entire gap, there is upwelling in the outer regions of the shear layers of both cylinders. Downdraft near the separation points begins around $z/D = -2$, marked by dashed circles. The velocity scale is exaggerated for better visibility. The minimum vertical velocity is approximately $W/U_0 = -0.45$. Panels show (*a*) $z/D = 0$, (*b*) $z/D = -2$, (*c*) $z/D = -4$, (*d*) $z/D = -6$, (*e*) $z/D = -8$ and (*f*) $z/D = -10$.

pressure of the downstream cylinder is lower for alternating overshoot/reattachment than for steady reattachment and bi-stable flow (Igarashi 1981). These observations correspond well with our result regarding the recirculation length. Note that the increase in L_r starts around $z/D = 1$, although in the instantaneous snapshots in figure 8, this region appears to fall within alternating the reattachment/overshoot regime. This is attributed to time variation of the boundaries between regimes and the cellular manifestation of modes.

A new finding in the present study is a streamwise secondary flow in the very near wake of the downstream cylinder, along the straight vertical extension. A positive streamwise velocity develops around $z/D = 1$, as shown in inset A in the lower right of figure 16. This secondary flow is associated with downstream displacement of the recirculation bubble clearly shown in figure 16(*c*). Although the scales are small, it is clear that the largest downstream displacement is found in the region of maximum upwelling velocity in the near wake. A related flow feature was described briefly by Gallardo *et al.* (2014), who reported that a near-zero, albeit negative, streamwise velocity plateau with a length of some $0.5D$ preceded the recirculation bubble.

Separation and reattachment lines, defined as zero shear stress iso-lines, are marked in figure 18. The reattachment point does not change significantly until $\beta \approx 21^\circ$, in the upper part of the curved gap, near $z/D = -3.5$. This is the region where symmetric

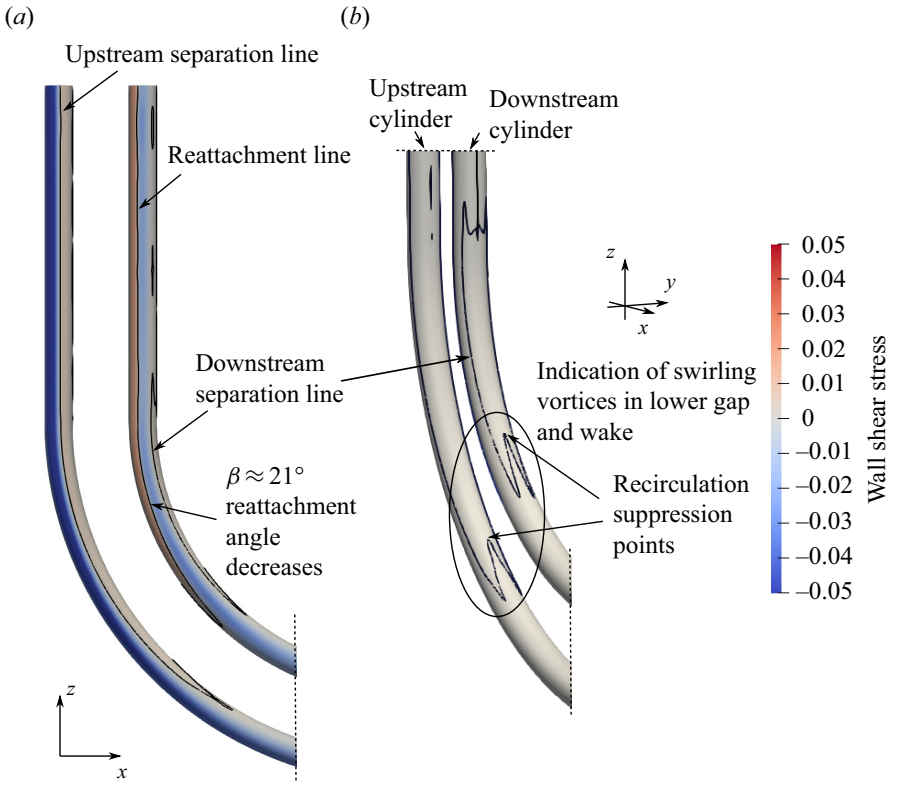

Figure 18. Time-averaged shear stress on the cylinder surfaces. (*a*) Side view (*b*) view from downstream. The black contour marks lines of zero shear stress. Here, θ_R is nearly constant until $\beta \approx 21°$.

reattachment gradually transitions to gap shedding. Along the vertical extension the value is $\theta_R = 68°$, very similar to straight tandem cylinders (Aasland *et al.* 2023). Separation from the downstream cylinder occurs near 135°. Note that, along most of the straight vertical extension, figure 18 shows no time-averaged separation line. This is due to the positive secondary streamwise flow in the near wake.

4. Discussion

Both Papaioannou *et al.* (2006) and Aasland *et al.* (2023) found that the flow in the gap of straight tandem cylinders within the reattachment regime has a basic spanwise cell structure. Aasland *et al.*'s (2023) study showed that this structure was very persistent in time, and could be easily discerned in the time-averaged velocity field. There is little evidence of such a structure in the present study, even along the straight vertical extension, although the instantaneous wake structure in the upper wake is similar to that of Aasland *et al.* (2023). This indicates that the axial flow does influence the three-dimensional instability in the gap and wake, even if the effect is slight.

Carmo *et al.* (2010*a*) found that mode T3 is a cooperative elliptical instability, 'cooperative' meaning that the instability depends on interaction between the shear layers. Mode T3 initiates in the gap, and placing a splitter plate directly upstream of the downstream cylinder can suppress it completely (Carmo *et al.* 2010*a*). The upwelling in the gap and near wake works in a similar way, reducing, although not entirely disrupting,

the communication between the shear layers. In this context, axial flow can be expected to act as a stabilising factor.

Within the co-shedding regime for tandem cylinders, the three-dimensional instability of the gap and wake is the same as for a single cylinder: mode A or mode B, depending on the Reynolds number (Carmo *et al.* 2010*a*). Moreover, while the downstream cylinder works as a stabiliser within the reattachment regime, it works as a de-stabiliser after the critical spacing (Papaioannou *et al.* 2006). This means that transition from mode A to mode B occurs earlier, in terms of Reynolds number, for tandem cylinders within the co-shedding regime than for a single cylinder. Intuitively, this should lead to a transition from mode T3 to mode B in the lower gap and wake of the present study, when the gap widens sufficiently to allow shedding. However, the vortex dislocations, as well as the strong downdraft in this region, alters the topology of the vortices to a point where visual observation is no longer useful to determine wavelengths etc. In order to finally determine the type of instability observed in the flow, a fully fledged stability analysis would be required, which is outside the scope of the present study. In this context, it is also important to note that the possible existence of critical points for higher Reynolds numbers than the present study is unknown. For straight tandem cylinders, no systematic studies of the three-dimensional wake instability exist for Reynolds numbers beyond 500 (Carmo, Meneghini & Sherwin 2010*b*), to the knowledge of the authors. Furthermore, the issue of critical points for the wake topology has not been addressed at all for single convex curved cylinders; a possible topic of further study.

The quasi-periodicity of the long-term gap flow asymmetry is a puzzle, since the bi-stable switch between tandem cylinder states is a random process. Thus, if it occurs periodically, it must be triggered by another periodic phenomenon. Zhu *et al.* (2019) observed a low-frequency switch between reattachment and co-shedding, which was assumed to be triggered by fluctuations of the axial velocity. Our own observations regarding the correlation between the cross-flow and vertical velocities (see figure 14) indicate a similar relation. As to the cause of the vertical velocity fluctuations, we believe it can be found in the lower gap. Previous studies of single bluff bodies have found low-frequency modulation of the vortex formation length (Miau *et al.* 1999, 2004; Lehmkuhl *et al.* 2013; Cao & Tamura 2020). The occurrence of such processes in the lower gap may alter the vertical velocity in a quasi-periodic fashion, which is subsequently transmitted along the span. This hypothesis is supported by the spectral analysis, which shows that the energy of the low frequencies is strongest in the gap shedding region. However, low-frequency variation of the reattachment points seems to be an inherent trait of tandem cylinder flow at the present Reynolds number (Aasland *et al.* 2023). The velocity spectra in the gap of Aasland *et al.* (2022*a*) also have clearly defined low-frequency peaks around $fD/U_0 = 0.01$, indicating that such a phenomenon extends into the subcritical Reynolds number range. This means that a straightforward relationship between the low-frequency variations in the lower gap and the quasi-periodic asymmetry is nearly impossible to determine, although clearly there is interaction between the two.

We see from figure 16(*c*) that the vertical velocity in the symmetry plane is negative below $z/D \approx -1.5$. Assuming that information is carried along the span by means of the axial velocity, this implies that in this region information is convected away form the upper part of the gap, towards the lower part. Conversely, above the stagnation line of the vertical velocity, information is carried upwards. From figure 8, however, we see that, outside the symmetry plane, in the regions that roughly correspond to the lateral position of the shear layers, there is positive vertical velocity all throughout the gap. Thus, it is possible to convey information in both directions along the gap by means of the axial velocity.

Aasland *et al.* (2022*a*) observed low-frequency variations in the drag and vertical force on the downstream cylinder, and suggested that these variations may be caused by a slow meandering of the angle at which gap shedding starts (i.e. β_{GS}) in the lower gap. The reasoning was that a larger reattachment region leads to increased gap suction and *vice versa*. We have not been able to directly observe such a meandering, though the same type of low-frequency drag variation occurs in the present study (not shown). The mode changes in the lower gap, as described in § 3.3 impact the drag, and the dominant low frequencies of the forces correspond well to the low-frequency content in the lower gap. However, the phenomenon appears to be more complex than previously assumed, since mode switches may occur locally (described in § 3.3 and for straight tandem cylinders by Aasland *et al.* 2023).

Some previous studies of straight tandem cylinders have suggested that, within the reattachment regime, it is the frequency of the gap vortices that drives the frequency of the wake vortices (Xu & Zhou 2004; Aasland *et al.* 2022*b*), similar to the 'lock-in' effect found for straight tandem cylinders within the co-shedding regime. This hypothesis was implicitly challenged by Hosseini, Griffith & Leontini (2021). In their investigation, a third body was placed in the near wake of tandem cylinders at $L/D = 5$ and $Re = 200$, a combination of gap ratio and Re which normally results in co-shedding. Provided that this third body was placed within the region of absolute instability of the downstream cylinder, vortex shedding could be entirely suppressed in the gap, resulting in a reattachment regime instead. We are inclined to believe in the view put forward by Hosseini *et al.* (2021). This suggests that the gap vortices for relatively small gap ratios are driven by the vortex shedding from the downstream cylinder, and not the other way around. This upstream feedback can result from fluctuations in the pressure field. If so, this would entail that the vortex formation in both the upper and lower gap in the present study is driven by the vortices in the upper wake. This interpretation further explains why the gap vortices in the lower gap have the same dominant frequency as those of the upper gap, even if the lower gap vortices are stronger, in terms of vorticity.

Finally, the independence principle is clearly invalid for the present case. This is underlined by the change of reattachment regime type which occurs in the upper part of the curved geometry, where the normal velocity and the corresponding local Reynolds number are quite similar to the nominal values. Below $z/D = -4$, these values decrease rapidly, while the dominant frequency remains virtually unchanged. Both Papaioannou *et al.* (2006) and Carmo *et al.* (2010*b*) predict a critical spacing of $L/D \approx 3.8$ for $Re = 500$. Herein, a corresponding effective gap ratio occurs in the vicinity of $z/D = -5$. This is close to the point of recirculation suppression in the near wake, so that a true co-shedding regime does not exist. It is obvious that the axial flow cannot be ignored in any part of the flow. This corresponds to the results of Alam *et al.* (2022), who concluded that the independence principle is invalid within the reattachment and bi-stable range for non-parallel yawed tandem cylinders.

5. Summary and concluding remarks

In the present study, the flow around curved tandem cylinders in the convex configuration has been investigated by means of DNS, at a Reynolds number of 500 and a nominal gap ratio of 3.0. Due to a gradual change in the effective gap ratio along the curved part of the span, there is a variation of tandem cylinder flow regimes from alternating reattachment/overshoot, through symmetric reattachment until shedding of vortices commences in the lower part of the gap. Similar to a single curved cylinder in the convex

configuration, vortex shedding is inhibited in the lower near wake, due to strong downdraft. A non-shedding swirling vortex regime prevails in this region.

Axial flow and spanwise flow regime variation lead to an intricate wake topology, with alterations between parallel and oblique spanwise vortex shedding. Communication between the shear layers is partially inhibited by the axial flow, and this influences the three-dimensional instability mechanism of the gap and wake, so that the spanwise cellular structure, which is typical for straight tandem cylinders at moderate Reynolds numbers, no longer occurs. That being said, the large-scale vortex shedding is governed by the vortices along the straight vertical extension, whose dominant and secondary frequencies are the same as for straight tandem cylinders at the same Reynolds number.

Spanwise vortex dislocations occur by two distinct physical mechanisms, one being spanwise frequency differences in the gap and wake, the other being shedding of gap vortices into the lower wake. Both may be present in the flow simultaneously, and along with bending and tilting of the streamwise vortices, this leads to extremely complex flow patterns in the wake. The topology is further complicated by interaction between the lower wake and the vortices in the horizontal part of the gap, which have a strong streamwise component.

Our results indicate that the flow is multi-stable, predominantly due to the spanwise flow regime variation. Alternating reattachment/overshoot, which is the governing regime along the straight vertical extensions, is in itself a bi-stable flow, with cellular manifestations of one-sided gap vortex shedding. In a previous study of straight tandem cylinders (Aasland *et al.* 2023), this caused long-term asymmetric vortex formation in the gap, intermittently switching from side to side. In the present study, the same type of asymmetry occurs, but the switch is quasi-periodic. The frequency at which the switch occurs is mirrored by low-frequency variations of the velocity fluctuations is the lower gap, which we believe result from slow variation of the recirculation length in the gap shedding region. This low-frequency variation may be transmitted along the span by means of the vertical velocity component. The asymmetry switch is seen to be accompanied by a surge of the vertical velocity.

Given the sensitivity of a single curved cylinder to the curvature and inflow direction, it seems likely that the flow around curved tandem cylinders, which is inherently more complex, should also be sensitive to these parameters. Moreover, the present study was carried out at a transitional Reynolds number, and the effect of turbulent flow is yet to be clarified.

Supplementary material and movies. Supplementary material and movies are available at https://doi.org/10.1017/jfm.2023.933.

Acknowledgements. The authors would like to thank Dr J. Gallardo (PRDW, Santiago, Chile) for insightful discussions regarding the origin of the low-frequency variations.

Funding. This work is supported by the Research Council of Norway through the Public Sector PhD Scheme (grant no. 258721/H40), and the Norwegian Public Roads Administration, where the first author is an employee. Computational hours were granted by the Norwegian HPC project NN9191K.

Declaration of interest. The authors report no conflict of interest.

Author ORCIDs.
Tale E. Aasland https://orcid.org/0000-0002-8504-930X;
Fengjian Jiang https://orcid.org/0000-0002-5321-3275.

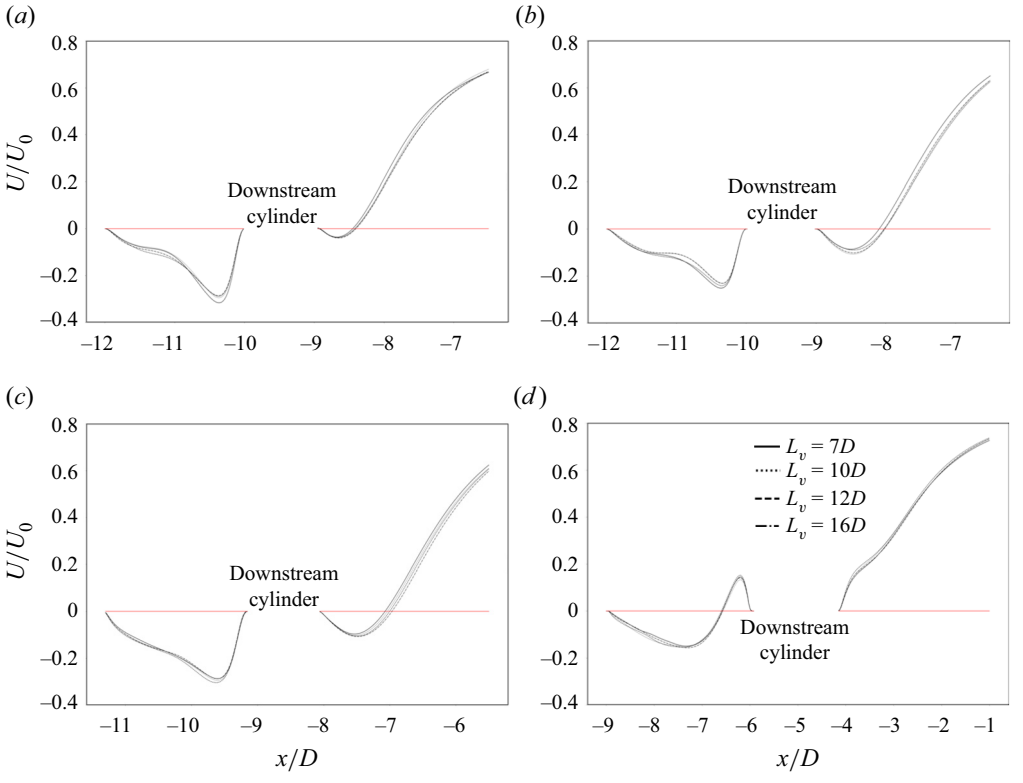

Figure 19. Comparison of time-averaged streamwise velocity profiles for different L_v at $y/D = 0$ and (*a*) $z/D = 5$, (*b*) $z/D = 0$, (*c*) $z/D = -4$ and (*d*) $z/D = -8$. In each of the plots, the horizontal extent of the downstream cylinder cross-section is cut out of the profiles.

Appendix. Effect of the straight vertical extension length

Because of spurious flow in the upper part of the domain discovered in the initial study (Aasland *et al.* 2022*a*), an investigation of the effect of L_v was carried out. Recalling that Gallardo *et al.* (2013) discovered that the main effect of vertical blockage was to suppress the upwelling in the near wake, the L_v parameter study focused on the time-averaged secondary flow features, which are all related to the vertical velocity component. Four different lengths were tested: $L_v = 7D$, $10D$, $12D$ and $16D$. For these simulations, sampling of statistics started after 250 time units, and was carried out for 550 time units, corresponding to some 100 von Kármán vortex shedding cycles.

The effect of the boundary condition is, naturally, most significant in the upper part of the domain. Horizontal profiles of the streamwise velocity, shown in figure 19, show that the influence penetrates rather far down into the domain, although the differences in recirculation length are small. Down to $z/D = -4$, a slight increase of the recirculation bubble was observed as L_v was increased. At $z/D = -8$, the differences are negligible.

Figure 20 shows the upwelling velocity along the straight vertical extension in the gap and wake. The adverse influence of the top boundary condition is evident in the profiles of $L_v = 7D$ and $10D$, especially in the gap. The same is true for the region of low positive streamwise velocity in the very near wake of the downstream cylinder, shown in figure 21. The effect is less prominent, although still visible, for $L_v = 12D$ and $16D$. Increased L_v seems to cause stronger upwelling in the gap, but weaker upwelling in

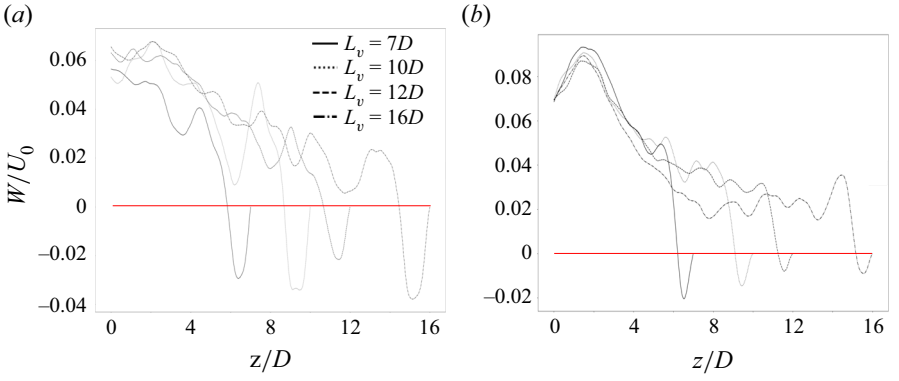

Figure 20. Effect of L_v on the upwelling in the near wake of the (a) upstream and (b) downstream cylinders. Panels show (a) $x/D = -11.8$ and (b) $x/D = 8.8$.

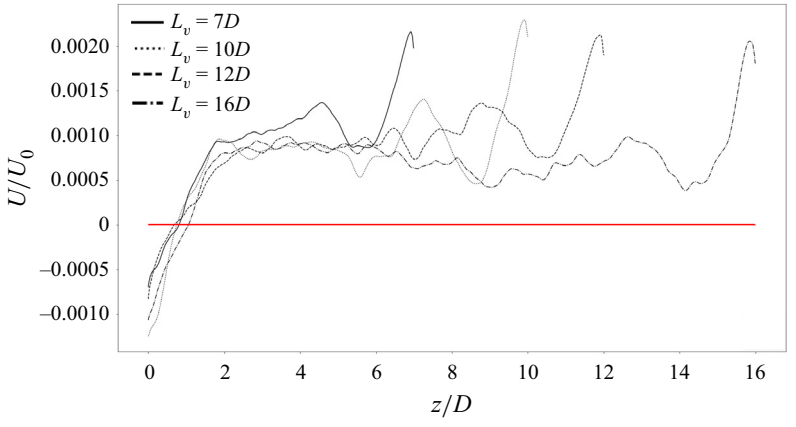

Figure 21. Effect of L_v on the positive U/U_0 in the very near wake of the downstream cylinder, at $x/D = -8.98$.

the wake, although the differences are smaller. Moreover, a slight decrease of St (based on the cross-flow forces) was found as L_v was increased, consistent with the increased recirculation length shown in figure 19. The values were $St = 0.152$, 0.149, 0148 and 0.146 for $L_v = 7D$, $10D$, $12D$ and $16D$, respectively.

There is no way to completely negate the blockage effect from the top boundary, so a compromise must be made between accuracy and computational cost. From figures 20 and 21, we see that, below $z/D = 5.0$, the influence from the upper boundary condition is small for $L_v = 12D$ and $L_v = 16D$. Further, the differences between the two L_v cases are small in this region. Thus, we conclude that $L_v = 12D$ gives acceptable accuracy vs cost for the present study.

References

Aasland, T.E., Pettersen, B., Andersson, H.I. & Jiang, F. 2022*a* Flow around curved tandem cylinders. *Trans. ASME J. Fluids Engng* **144** (12), 121301.

Aasland, T.E., Pettersen, B., Andersson, H.I. & Jiang, F. 2022*b* Revisiting the reattachment regime: a closer look at tandem cylinder flow at $Re = 10\,000$. *J. Fluid Mech.* **953**, A18.

AASLAND, T.E., PETTERSEN, B., ANDERSSON, H.I. & JIANG, F. 2023 Asymmetric cellular bistability in the gap between tandem cylinders. *J. Fluid Mech.* **966**, A39.

AFGAN, I., KAHIL, Y., BENHAMADOUCHE, S., ALI, M., ALKAABI, A., BERROUK, A.S. & SAGAUT, P. 2023 Cross flow over two heated cylinders in tandem arrangements at subcritical Reynolds number using large eddy simulations. *Intl J. Heat Fluid Flow* **100**, 109115.

AHMED, A. 2010 On the wake of a circular cylinder with nodal and saddle attachment. *J. Fluids Struct.* **26**, 41–49.

ALAM, M.M. 2014 The aerodynamics of a cylinder submerged in the wake of another. *J. Fluids Struct.* **51**, 393–400.

ALAM, M.M., RASTAN, M.R., WANG, L. & ZHOU, Y. 2022 Flows around two nonparallel tandem circular cylinders. *J. Wind Engng Ind. Aerodyn.* **220**, 104870.

ASSI, G.R.S., SRINIL, N., FREIRE, C.M. & KORKISCHKO, I. 2014 Wake dynamics of external flow past a curved circular cylinder with the free-stream aligned to the plane of curvature. *J. Fluids Struct.* **41**, 52–66.

CAO, Y. & TAMURA, T. 2020 Low-frequency unsteadiness in the flow around a square cylinder with critical angle of 14° and a Reynolds number if 2.2×10^4. *J. Fluids Struct.* **97**, 103087.

CARDELL, G.S. 1993 Flow past a circular cylinder with a permeable wake splitter plate. PhD thesis, California Institute of Technology.

CARMO, B.S. & MENEGHINI, J.R. 2006 Numerical investgation of the flow around two circular cylinders in tandem. *J. Fluids Struct.* **22**, 979–988.

CARMO, B.S., MENEGHINI, J.R. & SHERWIN, S.J. 2010*a* Secondary instabilities in the flow around two circular cylinders. *J. Fluid Mech.* **644**, 395–431.

CARMO, B.S., MENEGHINI, J.R. & SHERWIN, S.J. 2010*b* Possible states in the flow around two circular cylinders in tandem with separations in the vicinity of the drag inversion spacing. *Phys. Fluids* **22**, 054101.

CHIATTO, M., CARDINALE, C., SHANG, J.K. & GRASSO, F. 2023 Analysis of the wake flow behind concave curved cylinders with velocity measurements by particle image velocimetry and modal decomposition. *Phys. Fluids* **35**, 075153.

CHIATTO, M., SHANG, J.K., DE LUCA, L. & GRASSO, F. 2021 Insights into low Reynolds flow past finite curved cylinders. *Phys. Fluids* **33**, 035150.

DENG, J., REN, A.-L., ZOU, J.-F. & SHAO, X.-M. 2006 Three-dimensional flow around two circular cylinders in tandem arrangement. *Fluid Dyn. Res.* **38** (6), 386–404.

GALLARDO, J.P., ANDERSSON, H.I. & PETTERSEN, B. 2014 Turbulent wake behind a curved circular cylinder. *J. Fluid Mech.* **742**, 192–229.

GALLARDO, J.P., PETTERSEN, B. & ANDERSSON, H.I. 2013 Effect of free-slip boundary conditions on the flow around a curved circular cylinder. *Comput. Fluids* **86**, 389–394.

GAO, Y., HE, J., ONG, M.C., ZHAO, M. & WANG, L. 2021 Three-dimensional numerical investigation on flow past two side-by-side curved cylinders. *Ocean Engng* **234**, 109167.

GERRARD, J.H. 1966 The mechanics of the formation region of vortices behind bluff bodies. *J. Fluid Mech.* **25**, 401–413.

HENDERSON, R.D. 1997 Nonlinear dynamics and pattern formation in turbulent wake transition. *J. Fluid Mech.* **352**, 65–112.

HOSSEINI, N., GRIFFITH, M.D. & LEONTINI, J.S. 2021 Flow states and transitions in flows past arrays of tandem cylinders. *J. Fluid Mech.* **910**, A34.

IGARASHI, T. 1981 Characteristics of the flow around two circular cylinders arraged in tandem (1st report). *Bull. JSME* **24** (188), 323–330.

JIANG, F., PETTERSEN, B. & ANDERSSON, H.I. 2018*a* Influences of upstream extensions on flow around a curved cylinder. *Eur. J. Mech. (B/Fluids)* **67**, 79–86.

JIANG, F., PETTERSEN, B. & ANDERSSON, H.I. 2019 Turbulent wake behind a concave curved cylinder. *J. Fluid Mech.* **878**, 663–699.

JIANG, F., PETTERSEN, B., ANDERSSON, H.I., KIM, J. & KIM, S. 2018*b* Wake behind a concave curved cylinder. *Phys. Rev. Fluids* **3**, 094804.

KITAGAWA, T. & OHTA, H. 2008 Numerical investigation on flow around circular cylinders in tandem arrangement at a subcritical Reynolds number. *J. Fluids Struct.* **24**, 680–699.

LEE, S., PAIK, K.-J. & SRINIL, N. 2020 Wake dynamics of a 3D curved cylinder in oblique flows. *Intl J. Naval Arch. Ocean Engng* **12**, 501–517.

LEHMKUHL, O., RODRIGUES, I., BORRELL, R. & OLIVA, A. 2013 Low-frequency unsteadiness in the vortex formation region of a circular cylinder. *Phys. Fluids* **25**, 085109.

LIN, J.-C., YANG, Y. & ROCKWELL, D. 2002 Flow past two cylinders in tandem: instantaneous and averaged flow structure. *J. Fluids Struct.* **16** (8), 1059–1071.

LJUNGKRONA, L., NORBERG, C. & SUNDEN, B. 1991 Free-stream turbulence and tube spacing effect on surface pressure fluctuations for two tubes in an in-line arrangement. *J. Fluid Struct.* **5**, 701–727.

MA, B. & SRINIL, N. 2023 Prediction model for multidirectional vortex-induced vibrations of catenary riser in convex/concave and perpendicular flows. *J. Fluids Struct.* **117**, 103826.
MANHART, M. 2004 A zonal grid algorithm for DNS of turbulent boundary layers. *Comput. Fluids* **33**, 435–461.
MIAU, J.J., WANG, J.T., CHOU, J.H. & WEI, C.Y. 1999 Characteristics of low-frequency variations embedded in vortex-shedding process. *J. Fluids Struct.* **13**, 339–359.
MIAU, J.J., WU, S.J., HU, C.C. & CHOU, J.H. 2004 Low-frequency modulations associated with vortex shedding from flow over bluff body. *AIAA J.* **42**, 1388–1397.
MILIOU, A., DE VECCHI, A., SHERWIN, S.J. & GRAHAM, J.M.R. 2007 Wake dynamics of external flow past a curved cylinder with free stream aligned with the plane of curvature. *J. Fluid Mech.* **592**, 89–115.
MILIOU, A., SHERWIN, S.J. & GRAHAM, J.M.R. 2003*a* Fluid dynamic loading on curved riser pipes. *Trans. ASME J. Offshore Mech. Arctic Engng* **18** (1), 29–40.
MILIOU, A., SHERWIN, S.J. & GRAHAM, J.M.R. 2003*b* Wake topology of curved cylinders at low Reynolds numbers. *Flow Turbul. Combust.* **71**, 157–160.
NARASIMHAMURTHY, V.D., ANDERSSON, H.I. & PETTERSEN, B. 2009 Cellular vortex shedding behind a tapered circular cylinder. *Phys. Fluids* **21** (4), 044106.
OKAJIMA, A. 1979 Flows around two tandem circular cylinders at very high Reynolds numbers. *Bull. JSME* **22**, 504–511.
PAPAIOANNOU, G., YUE, D.K.P., TRIANTAFYLLOU, M. & KARNIADAKIS, G.E. 2006 Three-dimensionality effects in flow around two tandem cylinders. *J. Fluid Mech.* **558**, 387–413.
PELLER, N., LE DUC, A., TREMBLAY, T. & MANHART, M. 2006 High-order stable interpolations for immersed boundary methods. *Intl. J. Numer. Meth. Fluids* **53**, 1175–1193.
RAMBERG, S.E. 1983 The effects of yaw and finite length upon the vortex wakes of stationary and vibrating circular cylinders. *J. Fluid Mech.* **128**, 81–107.
SEYED-AGHAZADEH, B., BENNER, B., GJOKOLLARI, X. & MODERRES-SADEGHI, Y. 2021 An experimental investigation of vortex-induced vibration of a curved flexible cylinder. *J. Fluids Mech.* **927**, A21.
SEYED-AGHAZADEH, B., BUDZ, C. & MODARRES-SADEGHI, Y. 2015 The influence of higher harmonic flow forces on the response of a curved circular cylinder undergoing vortex-induced vibration. *J. Sound Vib.* **353**, 395–406.
SHANG, J.K., STONE, H.A. & SMITS, A.J. 2018 Flow past finite cylinders of constant curvature. *J. Fluid Mech.* **837**, 896–915.
SHI, X., ALAM, M. & BAI, H. 2020 Wakes of elliptical cylinders at low Reynolds number. *Intl J. Heat Fluid Flow* **82**, 108553.
SHIRAKASHI, M., HASEGAWA, A. & WAKIYA, S. 1986 Effect of secondary flow on Kármán vortex shedding from a yawed cylinder. *Bull. JSME* **29**, 1124–1132.
SRINIL, N., MA, B. & ZHANG, L. 2018 Experimental investigation on in-plane/out-of-plane vortex-induced vibrations of curved cylinder in parallel and perpendicular flows. *J. Sound Vib.* **421**, 275–299.
SUMNER, D. 2010 Two circular cylinders in cross-flow: a review. *J. Fluids Struct.* **26**, 849–899.
THAKUR, A., LIU, X. & MARSHALL, J.S. 2004 Wake flow of single and multiple yawed cylinders. *Trans. ASME J. Fluids Engng* **126**, 861–870.
UNGLEHRT, L., JENSSEN, U., KURZ, F., SCHANDERL, W., KREUZINGER, J., SCHWERTFIRM, F. & MANHART, M. 2022 Large-eddy simulation of the flow inside a scour hole around a circular cylinder using a cut cell immersed boundary method. *Flow Turbul. Combust.* **109**, 893–929.
DE VECCHI, A., SHERWIN, S.J. & GRAHAM, J.M.R. 2008 Wake dynamics of external flow past a curved circular cylinder with the free-stream aligned to the plane of curvature. *J. Fluids Struct.* **24**, 1262–1270.
WANG, D., LIU, Y., LI, H. & XU, H. 2021 Secondary instability of channel-confined transition around dual-circular cylinders in tandem. *Intl J. Mech. Sci.* **208**, 106692.
WANG, P., ZHOU, Q., ALAM, M.M., YANG, Y. & LI, M. 2022 Effects of streamwise gust amplitude on the flow around and forces on two tandem circular cylinders. *Ocean Engng* **261**, 112040.
WILKINS, S.J., HOGAN, J.D. & HALL, J.W. 2013 Vortex shedding in a tandem circular cylinder system with a yawed downstream cylinder. *Trans. ASME J. Fluids Engng* **135**, 071202.
WILLIAMSON, C.H.K. 1989 Oblique and parallel modes of vortex shedding in the wake of a circular cylinder at low Reynolds numbers. *J. Fluid Mech.* **206**, 579–627.
WILLIAMSON, C.H.K. 1992 The natural and forced formation of spot-like 'vortex dislocations' in the transition of a wake. *J. Fluid Mech.* **243**, 393–441.
WILLIAMSON, C.H.K. 1996 Vortex dynamics in the cylinder wake. *Annu. Rev. Fluid Mech.* **28**, 477–539.
XU, G. & ZHOU, Y. 2004 Strouhal numbers in the wake of two inline cylinders. *Exp. Fluids* **37**, 248–256.
YOUNIS, Y., ALAM, M & ZHOU, Y. 2016 Flow around two nonparallel tandem cylinders. *Phys. Fluids* **28** (12), 125106.

ZDRAVKOVICH, M.M. 1987 The effect of interference between circular cylinders in cross flow. *J. Fluids Struct.* **1**, 239–261.

ZHOU, Y. & ALAM, M. 2016 Wake of two interacting circular cylinders: a review. *Intl J. Heat Fluid Flow* **62**, 510–537.

ZHOU, Q., ALAM, M.M., CAO, S., LIAO, H. & LI, M. 2019 Numerical study of wake and aerodynamic forces on two tandem circular cylinders at $Re = 10^3$. *Phys. Fluids* **31**, 045103.

ZHU, H., WANG, R., BAO, Y., ZHOU, D., PING, H., HAN, Z. & SHERWIN, S.J. 2019 Flow over a symmetrically curved circular cylinder with the free stream parallel to the plane of curvature at low Reynolds number. *J. Fluids Struct.* **87**, 23–38.